

MOX–Report No. 14/2011

Non-Conforming High Order Approximations for the Elastic Wave Equation

ANTONIETTI, P.F.; MAZZIERI, I.; QUARTERONI, A.;
RAPETTI, F.

MOX, Dipartimento di Matematica “F. Brioschi”
Politecnico di Milano, Via Bonardi 9 - 20133 Milano (Italy)

mox@mate.polimi.it

<http://mox.polimi.it>

NON-CONFORMING HIGH ORDER
APPROXIMATIONS FOR THE ELASTIC WAVE
EQUATION

P.F. ANTONIETTI¹, I. MAZZIERI¹, A. QUARTERONI^{1,3},
F. RAPETTI²

March 31, 2011

¹ MOX– Modellistica e Calcolo Scientifico
Dipartimento di Matematica “F. Brioschi”
Politecnico di Milano
Piazza L. da Vinci 32, 20133 Milano, Italy
`paola.antonietti@polimi.it`, `ilario.mazzieri@mate.polimi.it`

² Université de Nice Sophia Antipolis, Laboratoire de Mathématiques J.A. Dieudonné,
Parc Valrose, Cedex 02, 06108 Nice, France.
`frapetti@unice.fr`

³ Chair of Modeling and Scientific Computing (CMCS),
Mathematics Institute of Computational Science and Engineering (MATHICSE),
École Polytechnique Fédérale de Lausanne (EPFL),
Station 8, 1015 Lausanne, Switzerland.
`alfio.quarteroni@epfl.ch`

Keywords: Spectral Methods; Non-conforming domain decomposition techniques; Computational seismology; Numerical approximations and analysis.

AMS Subject Classification: 65M55, 65M70, 35Q86.

Abstract

In this paper we formulate and analyse two non conforming high order strategies for approximating the solution of elastic wave problems in heterogeneous media, namely the Mortar Spectral Element Method and the Discontinuous Galerkin Spectral Element Method. Starting from a common variational formulation we make a full comparison of the two techniques from the points of view of accuracy, convergence, grid dispersion and stability.

1 Introduction and motivations

During the last decades there has been a growing and intensive research on the formulation and on the development of new algorithms for the numerical approximation of the elastic wave in the Earth. The possibility of inferring the physical parameter distribution of the Earth's substratum, from information provided by elastic wave propagations, has increased the interest towards computational seismology. Recent developments in this scientific discipline concern with different numerical strategies as finite differences, finite elements, but the major efforts apply to spectral element methods (see [26, 28, 22, 31, 46, 17, 30]).

A motivation is that, in geophysical or industrial applications, finite difference discretizations require very large system of equations to model realistic rock properties and uniform meshes are needed. On the other hand when finite element methods are employed for treating complex geometries, it is necessary to invert the mass matrix, that can be computationally very expensive.

The reasons for using spectral element based approximations can be summarized in the following lines. Firstly the flexibility in handling complex geometries, retaining the spatial exponential convergence for locally smooth solutions. Secondly, since spectral element methods are based on the weak formulation of the elastodynamic equations, they handle naturally both interface continuity and free boundary conditions, allowing very accurate resolutions of evanescent interface and surface waves (of major interest in seismology). Finally spectral element methods retain a high level parallel structure, thus well suited for parallel computers.

However when dealing with complex wave phenomena, such as soil-structure interaction problems or seismic response of sedimentary basins, the geometrical and polynomial flexibility is an important task for simulating correctly the wave-front field.

For this reason we consider two different non-conforming high-order techniques, namely the Mortar Spectral Element Method (MSEM), [10, 12], and the Discontinuous Galerkin Spectral Element Method (DGSEM), [7, 41, 43], to simulate seismic wave propagation in heterogeneous media. In contrast to standard conforming discretizations, as Spectral Element Method (SEM), [14, 15], these techniques have the further advantages that they can accommodate discontinuities, not only in the parameters, but also in the wavefield, while preserving the energy.

Depending on the involved materials it is possible to make a partition of the computational domain. Then, in each non-overlapping subregion a spectral finite element discretization is employed. The meshes, constituted by quadrilaterals or hexahedras, do not have to match between neighbouring subdomains, and different spectral approximation degrees are allowed in different subdomains. Therefore, the continuity of the solution at the skeleton of the decomposition is imposed weakly, either by means of a Lagrange multiplier for the MSEM, or by penalizing the jumps of displacements at that skeleton in the DGSEM.

In the present work, starting from a displacement based weak formulation of the elastodynamic equation, we study the MSEM and DGSEM coupled to second order time integration scheme, for the point of view of the accuracy, convergence, grid dispersion and stability.

In this context the grid dispersion criterion determines the greatest number of nodes per wavelength such that the numerical solution has an acceptable level of accuracy, while the stability criterion determines the largest time step allowed for explicit time integration schemes.

A general framework to study the numerical dispersion for the SEM was developed in [19] and analysed for the acoustic case up to third degree basis functions. In [45] was given a complete description for the elastic case, based on a Rayleigh quotient approximation of the eigenvalue problem characterizing the dispersion relation.

For the DGSEM, the grid dispersion has been analysed in [3, 21]. In particular in [3] the dispersion and dissipation errors of the acoustic wave equation in one space dimension are considered using the flux formulation. The results include third degree polynomial basis functions and conjectures on the extension to higher degrees are given. Making use of the plane wave analysis, in [21] a complete description of the grid dispersion properties is carried out for the acoustic and the elastic case.

For the MSEM it should be noted that, to the best of our knowledge, in the literature there are no available results for the grid dispersion properties regarding the elastic wave equation.

For what concerns the stability we remark that the classical numerical approach to solve a second order initial value problem is the Newmark method [29]. The Leap-Frog Finite Difference Method is a special case of the former scheme that is second order accurate, explicit and conditionally stable. This latter method is the most popular one in seismic modelling [31, 19, 18, 24, 16], but other schemes of Runge-Kutta or Taylor-Galerkin type are also available [20, 22, 30].

In this work we derive, for the Leap-Frog Method, specific stability bounds linking the time step with the size of the elements and the maximal velocity.

All results obtained are compared to the conforming SEM case.

The organisation of the paper is as follows. After introducing the elastodynamic problem and its variational formulation in Section 2, we describe in Section 3 the geometrical and functional discretization of the problem within the context of non conforming approximations. In particular we derive the Mortar and the Discontinuous Galerkin Spectral Formulations. The algebraic aspects of the two methods are then compared in Section 4. Section 5 is devoted to the grid dispersion and stability analysis, completely carried out for 2-D case. In Section 6 we discuss the property of accuracy and convergence of the MSEM and the DGSEM and finally we present a geophysical application, namely the seismic response of an alluvial basin.

2 Problem formulation

Let us consider an elastic medium occupying a finite region $\Omega \subset \mathbb{R}^d$, $d = 2, 3$, with boundary $\Gamma = \partial\Omega$ and unit outward normal \mathbf{n} . The boundary is assumed to be composed of portions Γ_D , where the displacement vector \mathbf{u} is prescribed, Γ_N where external loads apply, and Γ_{NR} where suitable non-reflecting conditions are imposed. The portion Γ_{NR} is in fact a fictitious boundary of the computational domain which is introduced to bound the physical domain for the numerical approximation of wave propagation problems in unbounded media. We make the assumptions that either Γ_D or Γ_N can be empty, $\Gamma_D \cap \Gamma_N = \emptyset$ and $\Gamma_N \cap \Gamma_{NR} = \emptyset$. Here and in the sequel, an underlying bar denotes matrix or tensor quantities, while vectors are typed in bold. Having fixed the temporal interval $(0, T)$, with T real and positive, the equilibrium equations for an elastic medium, subjected to an external force \mathbf{f} read:

$$\left\{ \begin{array}{ll} \rho \partial_{tt} \mathbf{u} - \nabla \cdot \underline{\sigma}(\mathbf{u}) = \mathbf{f}, & \text{in } \Omega \times (0, T), \\ \mathbf{u} = \mathbf{0}, & \text{on } \Gamma_D \times (0, T), \\ \underline{\sigma}(\mathbf{u}) \cdot \mathbf{n} = \mathbf{t}, & \text{on } \Gamma_N \times (0, T), \\ \text{non reflecting boundary conditions} & \text{on } \Gamma_{NR} \times (0, T), \\ \partial_t \mathbf{u} = \mathbf{u}_1, & \text{in } \Omega \times \{0\}, \\ \mathbf{u} = \mathbf{u}_0, & \text{in } \Omega \times \{0\}, \end{array} \right. \quad (1)$$

where \mathbf{u} is the medium displacement vector, $\underline{\sigma}$ the stress tensor, t the time variable and ρ the material density. Without loss of generality (see, for instance, [38]) we make the following further assumptions on Γ : on Γ_D the medium is rigidly fixed in the space and on Γ_N we prescribe surface tractions \mathbf{t} . Finally, on Γ_{NR} non-reflecting boundary conditions are imposed: from the mathematical point of view, the latter have the effect of introducing a fictitious traction \mathbf{t}^* which is a linear combination of space and time derivatives of the displacement \mathbf{u} (cf. [47, 16], for example). In particular for $d = 2$, if Γ_{NR} has outward unit normal $\mathbf{n} = (n_x, n_y)$ and tangential unit vector $\boldsymbol{\tau} = (\tau_x, \tau_y)$, the non-reflecting conditions in coordinate frame $\{\boldsymbol{\tau}, \mathbf{n}\}$ take the form

$$\left\{ \begin{array}{l} \frac{\partial}{\partial n}(\mathbf{u} \cdot \mathbf{n}) = -\frac{1}{c_P} \frac{\partial}{\partial t}(\mathbf{u} \cdot \mathbf{n}) + \frac{c_S - c_P}{c_P} \frac{\partial}{\partial \tau}(\mathbf{u} \cdot \boldsymbol{\tau}), \\ \frac{\partial}{\partial n}(\mathbf{u} \cdot \boldsymbol{\tau}) = -\frac{1}{c_S} \frac{\partial}{\partial t}(\mathbf{u} \cdot \boldsymbol{\tau}) + \frac{c_S - c_P}{c_P} \frac{\partial}{\partial \tau}(\mathbf{u} \cdot \mathbf{n}). \end{array} \right. \quad (2)$$

For $d = 3$ non-reflecting boundary conditions are given by

$$\left\{ \begin{array}{l} \frac{\partial}{\partial n}(\mathbf{u} \cdot \mathbf{n}) = -\frac{1}{c_P} \frac{\partial}{\partial t}(\mathbf{u} \cdot \mathbf{n}) + \frac{c_S - c_P}{c_P} \left[\frac{\partial}{\partial \tau_1}(\mathbf{u} \cdot \boldsymbol{\tau}_1) + \frac{\partial}{\partial \tau_2}(\mathbf{u} \cdot \boldsymbol{\tau}_2) \right], \\ \frac{\partial}{\partial n}(\mathbf{u} \cdot \boldsymbol{\tau}_1) = -\frac{1}{c_S} \frac{\partial}{\partial t}(\mathbf{u} \cdot \boldsymbol{\tau}_1) + \frac{c_S - c_P}{c_P} \frac{\partial}{\partial \tau_1}(\mathbf{u} \cdot \mathbf{n}), \\ \frac{\partial}{\partial n}(\mathbf{u} \cdot \boldsymbol{\tau}_2) = -\frac{1}{c_S} \frac{\partial}{\partial t}(\mathbf{u} \cdot \boldsymbol{\tau}_2) + \frac{c_S - c_P}{c_P} \frac{\partial}{\partial \tau_2}(\mathbf{u} \cdot \mathbf{n}), \end{array} \right. \quad (3)$$

where $\boldsymbol{\tau}_1$ and $\boldsymbol{\tau}_2$ are two arbitrary mutually orthogonal unit vectors on the plane orthogonal to \mathbf{n} , the normal to Γ_{NR} , such that $\{\boldsymbol{\tau}_1, \boldsymbol{\tau}_2, \mathbf{n}\}$ defines a right handed Cartesian frame.

The quantities c_P and c_S appearing in (2) and (3) are respectively the compressional and the shear wave velocities, defined as

$$c_P = \sqrt{\frac{\lambda + 2\mu}{\rho}} \quad \text{and} \quad c_S = \sqrt{\frac{\mu}{\rho}}, \quad (4)$$

where λ and μ are the Lamé elastic coefficients. We remark that for heterogeneous media ρ, λ and μ are bounded functions of the spatial variable, not necessarily continuous, i.e., ρ, λ and $\mu \in L^\infty(\Omega)$. We observe that Neumann type boundary conditions can be simply given by (2) or (3), where the right-hand side is substituted with the known value of the external load \mathbf{t} .

To complete the system in (1), we prescribe initial conditions \mathbf{u}_0 and \mathbf{u}_1 for the displacement and the velocity, respectively. When we consider viscoelastic materials, see Section 6, we introduce in the system (1) an additional term in the form of volume forces $\mathbf{f}^{visc} = -2\rho\zeta\dot{\mathbf{u}} - \rho\zeta^2\mathbf{u}$, where ζ is a suitable decay factor with dimension inverse of time. Correspondingly, the equation of motion becomes

$$\rho\partial_{tt}\mathbf{u} - \nabla \cdot \underline{\boldsymbol{\sigma}}(\mathbf{u}) = \mathbf{f} + \mathbf{f}^{visc}. \quad (5)$$

The parameter ζ is spatially variable (i.e. piecewise constant), as in [16], in order to model absorbing regions, thus providing an alternative or a complement to the absorbing boundary conditions. In other cases, like seismic wave propagation through heterogeneous media with strong elastic impedance, this model is used to prevent the onset of non-physical oscillations of the numerical solution.

We consider the strain tensor $\underline{\boldsymbol{\varepsilon}}$ defined as the symmetric gradient of \mathbf{u} , i.e.,

$$\underline{\boldsymbol{\varepsilon}}(\mathbf{u}) = \frac{1}{2}(\nabla\mathbf{u} + \nabla\mathbf{u}^\top),$$

so that the stress tensor $\underline{\boldsymbol{\sigma}}$ satisfies the constitutive relation (Hooke's law)

$$\underline{\boldsymbol{\sigma}}(\mathbf{u}) = \lambda\nabla \cdot \mathbf{u}\mathbf{I} + 2\mu\underline{\boldsymbol{\varepsilon}}(\mathbf{u}),$$

where \mathbf{I} is the d -dimensional identity tensor. Here and in the sequel we use the standard notation [1] to define the L^2 -inner product $(\cdot, \cdot)_\Omega$ for scalar, vector and tensor quantities.

By multiplying the first equation in (1) for a regular enough function \mathbf{v} (candidate to represent an admissible displacement), integrating by parts over the domain Ω , using the Green's formula:

$$-(\nabla \cdot \underline{\boldsymbol{\sigma}}(\mathbf{u}), \mathbf{v})_\Omega = (\underline{\boldsymbol{\sigma}}(\mathbf{u}), \underline{\boldsymbol{\varepsilon}}(\mathbf{v}))_\Omega - (\mathbf{v}, \underline{\boldsymbol{\sigma}}(\mathbf{u}) \cdot \mathbf{n})_\Gamma,$$

and imposing the boundary conditions, the variational formulation of (1) reads: $\forall t \in (0, T]$ find $\mathbf{u} = \mathbf{u}(t) \in V$ such that

$$d_{tt}(\rho\mathbf{u}, \mathbf{v})_\Omega + \mathcal{A}(\mathbf{u}, \mathbf{v})_\Omega = \mathcal{L}(\mathbf{v}) \quad \forall \mathbf{v} \in V, \quad (6)$$

where the bilinear form $\mathcal{A} : V \times V \rightarrow \mathbb{R}^d$ is defined as

$$\mathcal{A}(\mathbf{u}, \mathbf{v})_\Omega = (\underline{\sigma}(\mathbf{u}), \underline{\varepsilon}(\mathbf{v}))_\Omega,$$

and the linear functional $\mathcal{L} : V \rightarrow \mathbb{R}^d$ as

$$\mathcal{L}(\mathbf{v}) = (\mathbf{t}, \mathbf{v})_{\Gamma_N} + (\mathbf{t}^*, \mathbf{v})_{\Gamma_{NR}} + (\mathbf{f}, \mathbf{v})_\Omega.$$

Here V is the Sobolev space $V = \{\mathbf{v} \in [H^1(\Omega)]^d : \mathbf{v} = \mathbf{0} \text{ on } \Gamma_D\}$, where $L^2(\Omega)$ is the space of square integrable functions over Ω and $H^1(\Omega)$ is the space of functions in $L^2(\Omega)$ with gradient in $[L^2(\Omega)]^d$. We recall that the bilinear form $\mathcal{A}(\cdot, \cdot)$ is symmetric, V -elliptic and continuous [40]. These conditions imply that problem (6) admits a unique solution $\mathbf{u} \in \mathcal{C}^0((0, T); V) \cap \mathcal{C}^1((0, T); [L^2(\Omega)]^d)$ satisfying stability estimates [13, 40], provided that $\rho \in L^\infty(\Omega)$ is a strictly positive function, and that $\mathbf{u}_0 \in V$, $\mathbf{u}_1 \in [L^2(\Omega)]^d$ and $\mathbf{f} \in [L^2(\Omega \times (0, T))]^d$. By introducing a finite dimensional space V_δ which is a suitable approximation of V , the semi-discrete approximation of (6) reads : $\forall t \in (0, T]$ find $\mathbf{u}_\delta = \mathbf{u}_\delta(t) \in V_\delta$ such that

$$d_{tt}(\rho \mathbf{u}_\delta, \mathbf{v})_\Omega + \mathcal{A}(\mathbf{u}_\delta, \mathbf{v})_\Omega = \mathcal{L}(\mathbf{v}) \quad \forall \mathbf{v} \in V_\delta. \quad (7)$$

In the next section we will explain how to construct V_δ for two different families of non-conforming domain decomposition methods, namely, the Mortar Spectral Element Method (MSEM) and the Discontinuous Galerkin Spectral Element Method (DGSEM). Both methods are well suited to allow: 1) variable approximation orders, that is an elementwise polynomial degree, 2) unstructured and non-matching meshes, and 3) exponential rates of convergence in case of smooth solutions, [19].

3 Non-conforming Galerkin Spectral Formulations

In a domain decomposition approach we start by a discretization of the spatial differential operators in Ω , that relies on a time-independent three-level spatial decomposition of the domain Ω , as follows. At the first level, we subdivide Ω into K non overlapping regions Ω_k , $k = 1, \dots, K$, such that $\bar{\Omega} = \bigcup_{k=1}^K \bar{\Omega}_k$ with $\Omega_k \cap \Omega_\ell = \emptyset$ if $k \neq \ell$ and we define the skeleton of this (macro) decomposition as $\mathcal{S} = \bigcup_{k=1}^K \partial\Omega_k \setminus \partial\Omega$. Note that this (macro) decomposition can be geometrically non-conforming, *i.e.*, for two neighbouring subdomains Ω_k , Ω_ℓ , the interface $\gamma = \partial\Omega_k \cap \partial\Omega_\ell$ may not be a complete side (for $d = 2$) or face (for $d = 3$) of Ω_k or Ω_ℓ . Then problem (1) is solved in each Ω_k together with transmission conditions to ensure that the local solution is the restriction to $\Omega_k \times (0, T]$ of the global solution. For the elastic problem (1) the transmission conditions read: **(TC1)** $[[\mathbf{u}]] = 0$ and **(TC2)** $[[\underline{\sigma}]] = \mathbf{0}$, where $[[\]]$ denotes the jump of a quantity across a given interface.

To get the second level, in each Ω_k we introduce a partitioning \mathcal{T}_{h_k} , made by elements Ω_k^j (quadrilaterals if $d = 2$ or hexahedra if $d = 3$), with typical linear

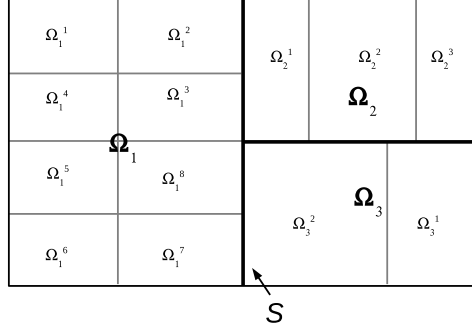


Figure 1: Example of a two dimensional subdomain partitioning. In this case $K = 3$ and $\overline{\Omega} = \overline{\Omega}_1 \cup \overline{\Omega}_2 \cup \overline{\Omega}_3$, with $\overline{\Omega}_1 = \bigcup_{j=1}^8 \overline{\Omega}_1^j$, $\overline{\Omega}_2 = \bigcup_{j=1}^3 \overline{\Omega}_2^j$ and $\overline{\Omega}_3 = \bigcup_{j=1}^3 \overline{\Omega}_3^j$.

size h_k and $\overline{\Omega}_k = \bigcup_{j=1}^{J_k} \overline{\Omega}_k^j$ (see Figure 1). Let us set $\widehat{\Omega} = (-1, 1)^d$ and suppose that there exists a suitable invertible mapping $F_k^j : \widehat{\Omega} \rightarrow \Omega_k^j$ with (positive) Jacobian $J_{\Omega_k^j}$. This (meso) partition is instead geometrically conforming, thus the intersection of two elements $\Omega_k^j, \Omega_k^\ell$, $\ell \neq j$, is either empty, or a vertex, or an edge, or a face of both Ω_k^j and Ω_k^ℓ . We thus have that

$$\int_{\Omega_k} f(\mathbf{x}) d\mathbf{x} = \sum_{\Omega_k^j \in \mathcal{T}_{h_k}} \int_{\Omega_k^j} f(\mathbf{x}) d\mathbf{x} = \sum_{\Omega_k^j \in \mathcal{T}_{h_k}} \int_{\widehat{\Omega}} (f \circ F_k^j)(\widehat{\mathbf{x}}) J_{\Omega_k^j}(\widehat{\mathbf{x}}) d\widehat{\mathbf{x}}.$$

The third (micro) level will be represented by the so-called Gauss-Lobatto-Legendre (GLL) points in each mesh element Ω_k^j . Let $\widehat{\mathbf{Q}}_{N_k}(\widehat{\Omega})$ be the space of functions defined on $\widehat{\Omega}$ that are algebraic polynomials of degree less than or equal to $N_k \geq 2$ in each variable x_1, \dots, x_d , and

$$\mathbf{Q}_{N_k}(\Omega_k^j) = \{v = \widehat{v} \circ F_k^j : \widehat{v} \in \widehat{\mathbf{Q}}_{N_k}(\widehat{\Omega})\}.$$

We define the finite dimensional space

$$X_\delta(\Omega_k) = \{v_\delta \in C^0(\overline{\Omega}_k) : v_{\delta|\Omega_k^j} \in \mathbf{Q}_{N_k}(\Omega_k^j), \forall \Omega_k^j \in \mathcal{T}_{h_k}\},$$

and finally

$$V_\delta = \{\mathbf{v}_\delta \in [L^2(\Omega)]^d : \mathbf{v}_{\delta|\Omega_k} \in [X_\delta(\Omega_k)]^d, \forall k = 1, \dots, K : \mathbf{v}_{\delta|\Gamma_D} = \mathbf{0}\},$$

where $\delta = \{\mathbf{h}, \mathbf{N}\}$ with $\mathbf{h} = (h_1, \dots, h_K)$ and $\mathbf{N} = (N_1, \dots, N_K)$ K -uplets of discretization parameters. Each component h_k and N_k represents the mesh size and the degree of the polynomial interpolation in the region Ω_k , respectively. In order to construct a nodal basis for V_δ , we introduce on each element Ω_k^j a set

of interpolation points $\{\mathbf{p}_i\}$ and corresponding degrees of freedom which allow to identify uniquely a generic function in V_δ . We remark the fact that, by the definition of the space V_δ , the basis functions will not be globally continuous on the whole domain Ω . In the spectral element approximation, the interpolation points are the GLL points. On the reference element $\widehat{\Omega}$, these points are tensor product of points defined in the interval $[-1, 1]$ as the zeros of $(1-x^2)L'_{N_k}$ where L'_{N_k} is the derivative of the Legendre polynomial L_{N_k} . This means that there exist N_k+1 points \mathbf{p}_i for the interpolation of a polynomial of degree N_k in $[-1, 1]$, [15]. As previously observed, in higher dimensions, the spectral nodes $\{\mathbf{p}_i\}$ are defined on the reference element $\widehat{\Omega}$ via tensor product of the one dimensional distribution, and are then mapped onto the generic element Ω_k^j in the physical space by F_k^j . In the SEM, the interpolation points are used also as quadrature points. Thus, we have

$$\int_{\widehat{\Omega}} (f \circ F_k^j)(\widehat{\mathbf{x}}) J_{\Omega_k^j}(\widehat{\mathbf{x}}) d\widehat{\mathbf{x}} \approx \sum_{i=1}^{(N_k+1)^d} (f \circ F_k^j)(\mathbf{p}_i) J_{\Omega_k^j}(\mathbf{p}_i) w_i,$$

where w_i are the weights of the GLL quadrature formula which is exact for all $(f \circ F_k^j) J_{\Omega_k^j} \in \mathbf{Q}_{2N_k-1}(\widehat{\Omega})$. The spectral shape functions $\Psi_i \in V_\delta$ are defined as $\Psi_i(\mathbf{p}_j) = \delta_{ij}$, $i, j = 1, \dots, (N_k+1)^d$, where δ_{ij} is the Kronecker symbol. It is straightforward to see that the restriction of any spectral function to Ω_k^j either coincides with a Lagrange polynomial or vanishes. Moreover the support of any shape function is limited to the neighbouring elements if the spectral node lies on the interface between two or more elements, while it is limited to only one element for internal nodes.

To introduce the non-conforming Mortar and Discontinuous Galerkin Variational Formulation, we write the equilibrium equations for a generic Ω_k , integrate it by parts and sum over $\Omega_k^j \in \mathcal{T}_{h_k}$. What we obtain is an equivalent form of the equation (6): For each $t \in (0, T]$, we now seek for a K -uplet $(\mathbf{u}_{\delta,1}, \dots, \mathbf{u}_{\delta,K})$ of functions, one for each subdomain Ω_k . Problem (7) is then equivalent to: $\forall t \in (0, T]$ find $(\mathbf{u}_{\delta,1}(t), \dots, \mathbf{u}_{\delta,K}(t)) \in V_\delta$ such that

$$\sum_{k=1}^K \text{d}t (\rho \mathbf{u}_{\delta,k}, \mathbf{v}_k)_{\Omega_k} + \mathcal{A}(\mathbf{u}_{\delta,k}, \mathbf{v}_k)_{\Omega_k} + \mathcal{B}(\mathbf{u}_{\delta,k}, \mathbf{v}_k)_{\partial\Omega_k \setminus \partial\Omega} = \sum_{k=1}^K \mathcal{L}(\mathbf{v}_k)_{\Omega_k}, \quad (8)$$

for all $(\mathbf{v}_1, \dots, \mathbf{v}_K) \in V_\delta$, where

$$\mathcal{A}(\mathbf{u}, \mathbf{v})_{\Omega_k} = (\underline{\sigma}(\mathbf{u}), \underline{\varepsilon}(\mathbf{v}))_{\Omega_k}, \quad \text{and} \quad \mathcal{B}(\mathbf{u}, \mathbf{v})_{\partial\Omega_k \setminus \partial\Omega} = (\underline{\sigma}(\mathbf{u}) \cdot \mathbf{n}, \mathbf{v})_{\partial\Omega_k \setminus \partial\Omega}. \quad (9)$$

Depending on the chosen non-conforming approach, the functional space V_δ is completed by additional conditions on $\mathbf{u}_{\delta,k}$, $k = 1, \dots, K$, on the skeleton of the macro decomposition which ensure that $\mathbf{u}_{\delta,k}$ is the restriction to Ω_k of $\mathbf{u}_\delta \in H^1(\Omega)^d$. The bilinear form $\mathcal{B}(\cdot, \cdot)$ may either be zero or gather all the contributions $(\sigma(\mathbf{u}_{\delta,k}) \cdot \mathbf{n}_k, \mathbf{v}_k)_{\partial\Omega_k \setminus \partial\Omega}$, $k = 1, \dots, K$, depending on the chosen

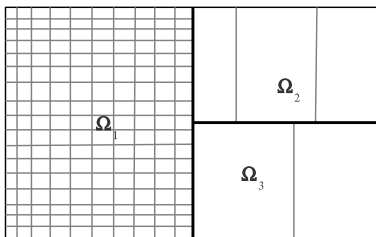


Figure 2: Example of non conforming decomposition.

approach. In fact, **TC1** is imposed by introducing a weak continuity condition on \mathcal{S} compatible with the considered formulations while **TC2** is enforced strongly. In both situations this lead to a strongly consistent numerical method. This means that the exact solution satisfies the numerical scheme for each choice of \mathbf{h} and \mathbf{N} , [37].

Equation (8) represents the starting point to introduce the Mortar Variational Formulation and the Discontinuous Variational Formulation. With both formulations we will be able to treat more general situations like (i) geometric non-conformity and (ii) polynomial degree non-conformity.

In (i) the partitions \mathcal{T}_k and \mathcal{T}_ℓ , of different regions Ω_k and Ω_ℓ can have mesh sizes h_k and h_ℓ significantly different: in fact, the practical importance of the proposed methods for elastodynamic problems lies on the possibility of using computational grids with very different local mesh sizes to take into account sharp variations in the physical parameters of the media.

Furthermore, the vertices of elements Ω_k^j and Ω_ℓ^i lying on the skeleton \mathcal{S} do not necessarily have to match, not even in the case $h_k = h_\ell$ (Figure 2).

In (ii) we use different polynomial approximation degrees in each region to get higher precision without refining too much the grid. Moreover, as we show in Section 5, it is evident that high order methods do not significantly suffer from numerical dispersion. The combination of (i) and (ii) yields approximated solutions that are both numerically accurate and computationally cheap.

Obviously, interface conditions other than those we consider are possible as well: an intuitive alternative is offered by pointwise matching conditions which require different spectral solutions to match on a particular set of points lying on \mathcal{S} . The Mortar or Discontinuous Galerkin approach is preferred to the pointwise matching since it brings optimal convergence rate, which is not the case for methods based on pointwise conditions (see [9] for the elliptic case), without affecting significantly the computational cost.

In the sequel, we describe in detail the non-conforming methods. To ease the presentation, we suppose that each partition \mathcal{T}_{h_k} of Ω_k consists in only one element, this means that each region is a spectral element. The more general case follows from similar arguments.

3.1 Mortar Spectral Formulation

In this section we introduce the mortar spectral element method for the solution of (8). The emphasis is on the numerical formulation, implementation and on the illustration of its flexibility and accuracy. To illustrate the key points, we consider the *free-vertex* variant of the MSEM [23, 8]. The *constrained-vertex* strategy can be implemented in a similar framework. For this latter technique the theoretical analysis is given in [10, 9, 32].

The MSEM relaxes the H^1 -continuity requirements of the conforming spectral-element method by considering each element (or in the general case each region) individually and achieving matching or patching conditions through a variational process. The *mortars* play the role of gluing the bricks of the spectral construction. Through the use of *mortars*, one can also couple domains where spectral elements are employed with others treated by finite elements [9]. However, in this context we focus on nonconforming spectral methods.

To begin, we denote by Γ_k^ℓ , $\ell = 1, \dots, 2d$, the edges (faces) of each subdomain Ω_k , $k = 1, \dots, K$, so that

$$\partial\Omega_k = \bigcup_{\ell=1}^{2d} \bar{\Gamma}_k^\ell.$$

We then identify the skeleton \mathcal{S} as the union of elementary non-empty components called *mortars* (or *masters*), more precisely

$$\mathcal{S} = \bigcup_{k=1}^K (\partial\Omega_k \setminus \partial\Omega) = \bigcup_{m=1}^M \bar{\gamma}_m, \quad \text{with } \gamma_m \cap \gamma_n = \emptyset, \quad \text{if } m \neq n,$$

where each mortar is a whole edge (or face) $\Gamma_{k(m)}^{\ell(m)}$ of a specific element $\Omega_{k(m)}$ and m is an arbitrary numbering $m = 1, \dots, M$, with M a positive integer. Those edges or faces Γ_k^ℓ that do not coincide with a mortar are called *non-mortars* (or *slaves*) and provide a dual description of the skeleton, as

$$\mathcal{S} = \bigcup_{m \text{ mortar}} \gamma_m^+ = \bigcup_{n \text{ non mortar}} \gamma_n^-.$$

The intersection of the closures of the mortars defines a set of vertices or *cross-points*

$$\mathcal{V} = \{\mathbf{x}_q = (\bar{\gamma}_r^+ \cap \bar{\gamma}_s^+), \mathbf{x}_q \notin \bar{\gamma}_m^+, m = 1, \dots, M\},$$

where q is an arbitrary numbering $q = 1, \dots, \tilde{\mathbf{v}}$. We define as well the set $\tilde{\mathcal{V}}$ of *virtual* vertices (that are not cross-points) as

$$\tilde{\mathcal{V}} = \{\tilde{\mathbf{x}}_q = (\bar{\gamma}_r^+ \cap \gamma_s^+)\},$$

where q is an arbitrary numbering $q = 1, \dots, \tilde{\mathbf{v}}$ (see Figure 3).

We define $\Lambda_\delta(\Gamma_k^\ell) = \mathbf{Q}_{N_k}(\Gamma_k^\ell)$, the space of the traces of functions of $X_\delta(\Omega_k)$ over Γ_k^ℓ and we also introduce $\hat{\Lambda}_\delta(\Gamma_k^\ell) = \mathbf{Q}_{N_k-2}(\Gamma_k^\ell)$.

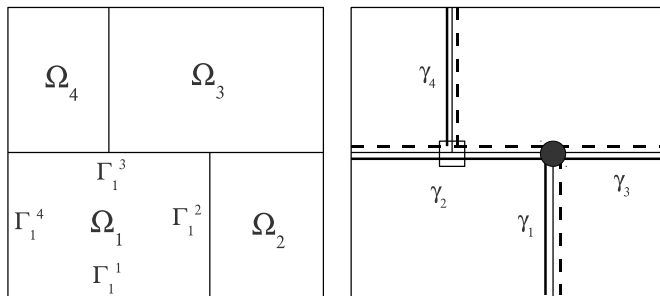


Figure 3: Nonconforming domain decomposition (left) and skeleton structure (right) showing a cross-point (\bullet), a virtual vertex (\square), the mortars (dark continuous lines) and the non-mortars (dark dashed lines).

We can now define the nonconforming spectral element discretization space \tilde{V}_δ as the space of functions $\mathbf{v}_\delta \in V_\delta$ that satisfy the following additional *mortar matching condition*:

- (MC1) let Φ be the *mortar function* associated with \mathbf{v}_δ , i.e., a function that is continuous on \mathcal{S} , zero on $\partial\Omega$ and such that on each mortar $\gamma_m = \Gamma_{k(m)}^{\ell(m)}$ it coincides with the restriction of $\mathbf{v}_{\delta,k} = \mathbf{v}_{\delta|\Omega_k}$ to γ_m ; then, for all indices (k, ℓ) such that Γ_k^ℓ is contained in \mathcal{S} but $(k, \ell) \neq (k(m), \ell(m))$ for all $m = 1, \dots, M$ (that is for all indices (k, ℓ) such that Γ_k^ℓ is a *non-mortar*) we require that:

$$\int_{\Gamma_k^\ell} (\mathbf{v}_{\delta,k} - \Phi) \cdot \widehat{\Phi} d\gamma = 0 \quad \forall \widehat{\Phi} \in [\widehat{\Lambda}_\delta(\Gamma_k^\ell)]^d \quad (10)$$

and that

$$\mathbf{v}_{\delta|\Omega_k}(\mathbf{x}_q) = \Phi(\mathbf{x}_q), \quad \forall \mathbf{x}_q \in \mathcal{V} \cup \tilde{\mathcal{V}}. \quad (11)$$

The integral matching condition (10) represents a minimization of the jump of the functions at internal boundaries with respect to the L^2 -norm and is the counterpart in the Mortar framework of condition **TC1**. The vertex condition (11) ensures exact continuity at cross-points. The Mortar Spectral Formulation is obtained by solving in each region Ω_k the elastodynamic variational problem (8) with homogeneous Neumann boundary conditions on \mathcal{S} ($\underline{\sigma}(\mathbf{u}) \cdot \mathbf{n} = \mathbf{0}$ so that $\sum_k \mathcal{B}(\mathbf{u}, \mathbf{v})_{\partial\Omega_k \setminus \partial\Omega}$ is identically zero, i.e., **TC2** is satisfied), and enforcing weak continuity of the displacement on \mathcal{S} with *mortar condition* (10).

Thus, the semi-discrete Mortar Spectral Formulation reads: $\forall t \in (0, T]$ find $(\mathbf{u}_{\delta,1}(t), \dots, \mathbf{u}_{\delta,K}(t)) \in V_\delta^{\text{mortar}}$ such that

$$\sum_{k=1}^K d_{tt} (\rho \mathbf{u}_{\delta,k}, \mathbf{v}_k)_{\Omega_k} + \mathcal{A}(\mathbf{u}_{\delta,k}, \mathbf{v}_k)_{\Omega_k} = \sum_{k=1}^K \mathcal{L}(\mathbf{v}_k), \quad (12)$$

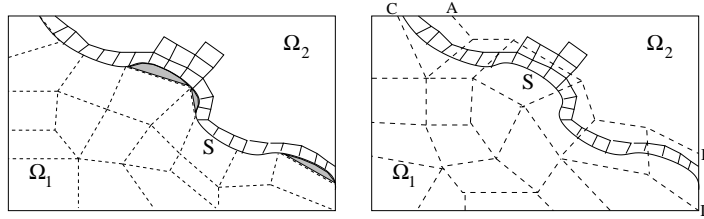


Figure 4: Example of rectangular domain Ω where the surface \mathcal{S} separates two different physical materials. Non overlapping subdomains and meshes (left), holes as non meshed regions (shaded areas) and overlapping subdomains and meshes (right).

for all $(\mathbf{v}_1, \dots, \mathbf{v}_K) \in V_\delta^{mortar}$ where

$$V_\delta^{mortar} = \{(\mathbf{v}_1, \dots, \mathbf{v}_K) \in V_\delta : \text{mortar condition MC1 is satisfied}\}.$$

The mortar element method was originally proposed as a non-overlapping domain decomposition approach, however recently it has been generalized to the case of overlapping subdomains [27, 33, 39]. The overlapping version may be quite useful in elastodynamic modelling to treat subdomains with complex shaped boundaries (see an application in Section 7). Let us consider the two cases presented in Figure 4.

On the one hand, the rectangular domain Ω is partitioned into two non-overlapping subdomains Ω_1 , Ω_2 and the skeleton \mathcal{S} of the decomposition coincides with the separation surface between two different materials such that elastic waves propagate faster in Ω_2 than in Ω_1 . By adapting the mesh size h_k in each subdomain Ω_k according to the propagation velocity of the elastic waves in the subdomain, one reasonably selects $h_1 > h_2$. However, h_2 has to be small enough to follow the shape of \mathcal{S} and h_1 cannot be too large otherwise some holes appear close to the surface \mathcal{S} . As a consequence, $h_1 \sim h_2$ in a neighbourhood of \mathcal{S} resulting in a large number of unknowns to consider in both subdomains. The mortar matching condition allows to transfer the displacement from the set of master interpolation points to the set of slave ones and both sets of points are located on the $(d-1)$ -dimensional surface \mathcal{S} . Note that numerical results are independent of the choice of the master and of the slave subdomains.

On the other hand, the rectangular domain Ω is partitioned into two overlapping subdomains, namely, Ω_1 which is the bottom left-handed region under the dashed polyhedral surface AB and Ω_2 the top right-handed region over the solid line \mathcal{S} . These two subdomains overlap in the region between \mathcal{S} and the surface AB . In this case, we can have $h_1 > h_2$ everywhere in Ω_1 and the mortar matching condition allows to transfer the displacement from the set of interpolation points of Ω_1 which are contained in the d -dimensional region bounded by the polyhedral surfaces AB and CD to the set of interpolation points of Ω_2 which are on the $(d-1)$ -dimensional surface \mathcal{S} . Indeed, in the overlapping case, the slave subdomain always covers the master one. Moreover, the slave

subdomain is chosen as the one where the mesh best describes the surface \mathcal{S} and the master subdomain contains the source of elastic waves. In the overlapping case, the matching condition reads:

(MCO1) let Φ be a function that is equal to $\mathbf{v}_{\delta,k}$ in the d -dimensional elements of master subdomain Ω_k containing a part of \mathcal{S} , and zero elsewhere. Then, for each slave subdomain Ω_i such that $\partial\Omega_i \cap \mathcal{S} \neq \emptyset$, we require that:

$$\int_{\mathcal{S}} (\mathbf{v}_{\delta,i} - \Phi) \cdot \widehat{\Phi} d\gamma = 0 \quad \forall \widehat{\Phi} \in [\Lambda_{\delta,i}(\mathcal{S})]^d \quad (13)$$

where $\Lambda_{\delta,i}(\mathcal{S})$ is the space of the traces over \mathcal{S} of functions belonging to $X_{\delta}(\Omega_i)$.

3.2 Discontinuous Galerkin Spectral Formulation

Before going into the detail of the Discontinuous Galerkin Spectral Formulation let us introduce some notation that will be useful in the sequel. Let us subdivide the skeleton \mathcal{S} in elementary components as follows:

$$\overline{\mathcal{S}} = \bigcup_{j=1}^M \overline{\gamma}_j, \quad \text{with } \gamma_i \cap \gamma_j = \emptyset, \quad \text{if } i \neq j,$$

where each element $\overline{\gamma}_j = (\partial\overline{\Omega}_{k(j)} \cap \partial\overline{\Omega}_{\ell(j)}) \setminus \partial\Omega$, for some different positive integers k and ℓ : this decomposition is unique (see Figure 5). Next we collect all the edges (faces if $d = 3$) in the set \mathcal{F}_I .

For any pair of neighbouring regions Ω_i and Ω_j that share a non trivial edge (face) $\gamma \in \mathcal{F}_I$, we denote by $\mathbf{v}_i, \underline{\sigma}_i$ (resp. $\mathbf{v}_j, \underline{\sigma}_j$) the restriction to Ω_i (resp. Ω_j) of regular enough functions $\mathbf{v}, \underline{\sigma}$. We also denote by \mathbf{n}_i (resp. \mathbf{n}_j) the exterior unit normal to Ω_i (resp. Ω_j).

On each $\gamma \in \mathcal{F}_I$ we define the average and jump operators for \mathbf{v} and $\underline{\sigma}$ as follows:

$$\{\mathbf{v}\} = \frac{1}{2}(\mathbf{v}_i + \mathbf{v}_j), \quad \llbracket \mathbf{v} \rrbracket = \mathbf{v}_i \otimes \mathbf{n}_i + \mathbf{v}_j \otimes \mathbf{n}_j, \quad (14)$$

and

$$\{\underline{\sigma}\} = \frac{1}{2}(\underline{\sigma}_i + \underline{\sigma}_j), \quad \llbracket \underline{\sigma} \rrbracket = \underline{\sigma}_i \cdot \mathbf{n}_i + \underline{\sigma}_j \cdot \mathbf{n}_j, \quad (15)$$

where $\mathbf{a} \otimes \mathbf{b} \in \mathbb{R}^{d \times d}$ is the tensor with entries $(\mathbf{a} \otimes \mathbf{b})_{ij} = a_i b_j, 1 \leq i, j \leq d$, for all $\mathbf{a}, \mathbf{b} \in \mathbb{R}^d$.

After integration by parts over each region, the application of jump and average operators defined in (14)-(15) and the imposition of condition **TC2**, i.e., continuity of traction across \mathcal{S} , we deduce that

$$\sum_{k=1}^K (\underline{\sigma}(\mathbf{u}) \cdot \mathbf{n}, \mathbf{v})_{\partial\Omega_k \setminus \partial\Omega} = \sum_{j=1}^M (\{\underline{\sigma}(\mathbf{u})\}, \llbracket \mathbf{v} \rrbracket)_{\gamma_j}. \quad (16)$$

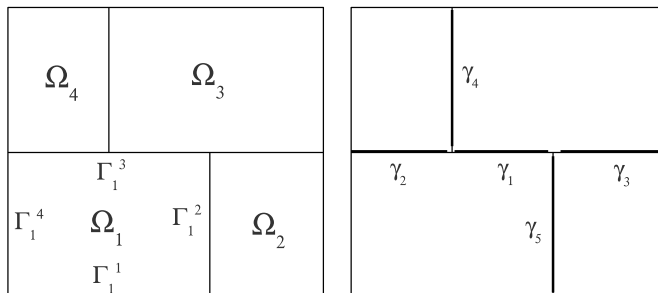


Figure 5: Nonconforming domain decomposition (left) and skeleton structure (right) showing the elementary components (dark continuous lines).

Since also **TC1** holds, i.e., $[[\mathbf{u}]] = \underline{0}$ is zero across \mathcal{S} , we can further add other terms in (16) that penalize and control the jumps of the numerical solution,

$$\sum_{j=1}^M \theta ([[\mathbf{u}_\delta]], \{ \underline{\sigma}(\mathbf{v}) \})_{\gamma_j} + \sum_{j=1}^M \eta_{\gamma_j} ([[\mathbf{u}_\delta]], [[\mathbf{v}]])_{\gamma_j},$$

with $\theta = \{-1, 0, 1\}$ and η_{γ_j} positive constants depending on the discretization parameters \mathbf{h} and \mathbf{N} and on the Lamé coefficients. The terms do not affect consistency of the method and are added with the purpose of providing more generality and better stability properties to the scheme (see [41, 42]).

In this context we choose $\eta_{\gamma_j} = \alpha \{ \lambda + 2\mu \}_A \mathbf{N}_j^2 / \mathbf{h}_j$, where $\{q\}_A$ represents the harmonic average of the quantity q , defined by $\{q\}_A = 2q_{k(j)}q_{\ell(j)} / (q_{k(j)} + q_{\ell(j)})$, $\mathbf{N}_j = \max(N_{k(j)}, N_{\ell(j)})$, $\mathbf{h}_j = \min(h_{k(j)}, h_{\ell(j)})$ and α is a positive constant at disposal. The semi-discrete DG Formulation reads:

$\forall t \in (0, T]$ find $\mathbf{u}_\delta = (\mathbf{u}_{\delta,1}(t), \dots, \mathbf{u}_{\delta,K}(t)) \in V_\delta^{DG} \equiv V_\delta$ such that

$$\sum_{k=1}^K \left(d_{tt}(\rho \mathbf{u}_\delta, \mathbf{v})_{\Omega_k} + \mathcal{A}(\mathbf{u}_\delta, \mathbf{v})_{\Omega_k} \right) + \sum_{j=1}^M \mathcal{B}(\mathbf{u}_\delta, \mathbf{v})_{\gamma_j} = \sum_{k=1}^K \mathcal{L}(\mathbf{v}_k), \quad (17)$$

for all $\mathbf{v} = (\mathbf{v}_1, \dots, \mathbf{v}_K) \in V_\delta^{DG}$, with

$$\mathcal{B}(\mathbf{u}, \mathbf{v})_{\gamma_j} = -(\{ \underline{\sigma}(\mathbf{u}) \}, [[\mathbf{v}]])_{\gamma_j} + \theta ([[\mathbf{u}]], \{ \underline{\sigma}(\mathbf{v}) \})_{\gamma_j} + \eta_{\gamma_j} ([[\mathbf{u}]], [[\mathbf{v}]])_{\gamma_j}. \quad (18)$$

Corresponding to different values of θ we obtain different DG schemes, namely: $\theta = -1$ (resp. $\theta = 1$) leads to the symmetric (resp. non-symmetric NIPG) interior penalty method SIPG, while $\theta = 0$ corresponds to the so-called incomplete interior penalty method IIPG (see [7, 41, 42, 43] for more details).

4 Algebraic formulations and time integration scheme

We discuss here the algebraic formulations of the two non-conforming approaches presented in the previous sections. In particular we describe how to construct the linear system coming from the mortar or the DG discretization and subsequently we introduce the time integration scheme employed for the numerical simulations.

4.1 Algebraic formulation of the problem

We consider the elastodynamic equation (1) in a bounded region $\Omega \subset \mathbb{R}^2$ with Dirichlet boundary condition, thus $\Gamma_D \equiv \partial\Omega$. To ease the presentation let also suppose that Ω is partitioned into K non-overlapping spectral elements $\Omega_1, \dots, \Omega_K$ so that $\bar{\mathcal{S}} = \bigcap_{k=1}^K \partial\bar{\Omega}_k \setminus \Gamma_D$. The more general case can be obtained in a similar manner.

We denote by $D = \sum_{k=1}^K (N_k + 1)^2$ the dimension of each component of V_δ and we introduce a basis $\{\Psi_i^1, \Psi_i^2\}_{i=1}^D$ for the finite dimensional space V_δ , where $\Psi_i^1 = (\Psi_i^1, 0)^\top$ and $\Psi_i^2 = (0, \Psi_i^2)^\top$. Dropping the subscript δ , we write the trial functions $\mathbf{u} \in V_\delta$ as linear combination of basis functions

$$\mathbf{u}(\mathbf{x}, t) = \sum_{j=1}^D \begin{bmatrix} \Psi_j^1(\mathbf{x}) \\ 0 \end{bmatrix} U_j^1(t) + \sum_{j=1}^D \begin{bmatrix} 0 \\ \Psi_j^2(\mathbf{x}) \end{bmatrix} U_j^2(t), \quad (19)$$

Next, we define $a_k = 1 + \sum_{j=1}^{k-1} (N_j + 1)^2$ and $b_k = \sum_{j=1}^k (N_j + 1)^2$ and we order the basis functions such that

$$\mathbf{u}|_{\Omega_k} = (u^1, u^2)|_{\Omega_k} = \left(\sum_{j=a_k}^{b_k} \Psi_j^1 U_{j,k}^1, \sum_{j=a_k}^{b_k} \Psi_j^2 U_{j,k}^2 \right)^\top, \quad (20)$$

for $k = 1, \dots, K$. With the notation just introduced, we write the equation (8) for any test function $\Psi_j^\ell(\mathbf{x})$, for $\ell = 1, 2$, in the space V_δ and we obtain the following set of discrete ordinary differential equations:

$$\underline{\mathbf{M}}\ddot{\mathbf{U}} + \underline{\mathbf{A}}\mathbf{U} + \underline{\mathbf{B}}\mathbf{U} = \mathbf{F}^{ext}, \quad (21)$$

or equivalently

$$\begin{bmatrix} \underline{\mathbf{M}}^1 & \underline{\mathbf{0}} \\ \underline{\mathbf{0}} & \underline{\mathbf{M}}^2 \end{bmatrix} \begin{bmatrix} \ddot{\mathbf{U}}^1 \\ \ddot{\mathbf{U}}^2 \end{bmatrix} + \begin{bmatrix} \underline{\mathbf{A}}^1 + \underline{\mathbf{B}}^1 & \underline{\mathbf{A}}^2 + \underline{\mathbf{B}}^2 \\ \underline{\mathbf{A}}^3 + \underline{\mathbf{B}}^3 & \underline{\mathbf{A}}^4 + \underline{\mathbf{B}}^4 \end{bmatrix} \begin{bmatrix} \mathbf{U}^1 \\ \mathbf{U}^2 \end{bmatrix} = \begin{bmatrix} \mathbf{F}^{ext,1} \\ \mathbf{F}^{ext,2} \end{bmatrix}, \quad (22)$$

where $\ddot{\mathbf{U}}$ represents the vector of nodal acceleration and \mathbf{F}^{ext} the vector of externally applied loads. As a consequence of assumptions on the basis functions, the mass matrices $\underline{\mathbf{M}}^1$ and $\underline{\mathbf{M}}^2$ have a block diagonal structure $\underline{\mathbf{M}}^\ell =$

$\text{diag}(\underline{\mathbf{M}}_1^\ell, \underline{\mathbf{M}}_2^\ell, \dots, \underline{\mathbf{M}}_K^\ell)$, for $\ell = 1, 2$, where each block $\underline{\mathbf{M}}_k^\ell$ is associated to the spectral element Ω_k and

$$\mathbf{M}_k^\ell(i, j) = (\rho \Psi_j^\ell, \Psi_i^\ell)_{\Omega_k}, \quad \text{for } i, j = a_k, \dots, b_k. \quad (23)$$

The matrix $\underline{\mathbf{A}}$ associated to the bilinear form $\mathcal{A}(\cdot, \cdot)$ defined in (9) takes the form

$$\underline{\mathbf{A}} = \begin{bmatrix} \underline{\mathbf{A}}^1 & \underline{\mathbf{A}}^2 \\ \underline{\mathbf{A}}^3 & \underline{\mathbf{A}}^4 \end{bmatrix},$$

where the block diagonal matrices $\underline{\mathbf{A}}^\ell$, for $\ell = 1, \dots, 4$ are equal to

$$\underline{\mathbf{A}}^\ell = \text{diag}(\underline{\mathbf{A}}_1^\ell, \underline{\mathbf{A}}_2^\ell, \dots, \underline{\mathbf{A}}_K^\ell).$$

The elements of the matrices $\underline{\mathbf{A}}_k^\ell$, for $\ell = 1, \dots, 4$ and $k = 1, \dots, K$ are defined by

$$\begin{aligned} \mathbf{A}_k^1(i, j) &= \mathcal{A}(\underline{\sigma}(\Psi_j^1), \underline{\varepsilon}(\Psi_i^1))_{\Omega_k}, & \mathbf{A}_k^2(i, j) &= \mathcal{A}(\underline{\sigma}(\Psi_j^2), \underline{\varepsilon}(\Psi_i^1))_{\Omega_k}, \\ \mathbf{A}_k^3(i, j) &= \mathcal{A}(\underline{\sigma}(\Psi_j^1), \underline{\varepsilon}(\Psi_i^2))_{\Omega_k}, & \mathbf{A}_k^4(i, j) &= \mathcal{A}(\underline{\sigma}(\Psi_j^2), \underline{\varepsilon}(\Psi_i^2))_{\Omega_k}, \end{aligned} \quad (24)$$

for $i, j = a_k, \dots, b_k$. We remark that the matrices $\underline{\mathbf{M}}$ and $\underline{\mathbf{A}}$ are very similar to those resulting from the discretization of the elastodynamic equation (6) with conforming methods like Spectral Element Method (see [14, 15]).

The matrix $\underline{\mathbf{B}}$, associated to the bilinear form $\mathcal{B}(\cdot, \cdot)$ defined in (9), is the one that takes into account the discontinuity of the numerical solution across the skeleton \mathcal{S} . In the DG approach it is expressed by

$$\underline{\mathbf{B}} = \begin{bmatrix} \underline{\mathbf{B}}^1 & \underline{\mathbf{B}}^2 \\ \underline{\mathbf{B}}^3 & \underline{\mathbf{B}}^4 \end{bmatrix},$$

where

$$\underline{\mathbf{B}}^\ell = \begin{bmatrix} \underline{\mathbf{B}}_{1,1}^\ell & \cdots & \underline{\mathbf{B}}_{1,K}^\ell \\ \vdots & \ddots & \vdots \\ \underline{\mathbf{B}}_{K,1}^\ell & \cdots & \underline{\mathbf{B}}_{K,K}^\ell \end{bmatrix}, \quad \text{for } \ell = 1, \dots, 4.$$

In particular the elements of each matrix $\underline{\mathbf{B}}_{k,n}^1$ are defined by:

$$\begin{aligned} \mathbf{B}_{k,n}^1(i, j) &= \sum_{\gamma \in \mathcal{F}_I} \mathcal{B}(\Psi_j^1, \Psi_i^1)_\gamma \\ &= \sum_{\gamma \in \mathcal{F}_I} - \int_\gamma \{\underline{\sigma}(\Psi_j^1)\} : [[\Psi_i^1]] ds + \theta \int_\gamma [[\Psi_j^1]] : \{\underline{\sigma}(\Psi_i^1)\} ds \\ &\quad + \eta_\gamma \int_\gamma [[\Psi_j^1]] : [[\Psi_i^1]] ds, \end{aligned}$$

for $i = a_k, \dots, b_k$ and $j = a_n, \dots, b_n$. The elements of the matrices $\underline{\mathbf{B}}_{k,n}^\ell$, for $\ell = 2, 3, 4$ are defined in a similar way.

The situation is a little bit more complicated in the Mortar approach, since the weak continuity condition across the skeleton \mathcal{S} does not appear explicitly in the variational equation but it is a constraint in the functional space V_δ^{mortar} : in fact, in the Mortar Variational Formulation, $\mathcal{B}(\cdot, \cdot) = 0$ implies that $\underline{\mathbf{B}}$ is a null matrix.

To account for **MC1** we need to modify (22) as follows. Without loss of generality let us suppose that γ_n^- is a non mortar edge contained in \mathcal{S} and moreover that it is shared by two regions Ω_m and Ω_n . We call *master* the side of γ_n^- belonging to $\bar{\Omega}_m$ and *slave* the other side. Thus, the *mortar conditions MC1* can be recast as:

- (i) $\Phi = \mathbf{u}_m$ on γ_n^- ,
- (ii) $\int_{\gamma_n^-} (\mathbf{u}_n - \mathbf{u}_m) \cdot \widehat{\Phi} ds = 0 \quad \forall \widehat{\Phi} \in [\widehat{\Lambda}_\delta(\gamma_n^-)]^d$.

Now, for the spectral element Ω_n (resp. Ω_m) we order first the $N_n + 1$ (resp. $N_m + 1$) degrees of freedom (d.o.f.) associated to the spectral nodes \mathbf{p}_i that live in γ_n^- and next the d.o.f. associated to the remaining spectral nodes \mathbf{p}_i . With this assumptions the restriction of the function \mathbf{u}_n on γ_n^- is rewritten as

$$\mathbf{u}_n|_{\gamma_n^-} = \left(\sum_{j=1}^{N_n+1} \Psi_j^1 U_{j,n}^1, \sum_{j=1}^{N_n+1} \Psi_j^2 U_{j,n}^2 \right),$$

and the same for the function $\mathbf{u}_m|_{\gamma_n^-}$. Hence, by definition of scalar product, the *mortar condition (ii)* becomes

$$\int_{\gamma_n^-} (u_n^1 - u_m^1) \widehat{\Phi}^1 ds + \int_{\gamma_n^-} (u_n^2 - u_m^2) \widehat{\Phi}^2 ds = 0 \quad \forall \widehat{\Phi}^1, \widehat{\Phi}^2 \in \widehat{\Lambda}_\delta(\gamma_n^-). \quad (25)$$

Since the integrals in (25) concern separately the two components of the displacement, we focus the attention onto one of them, dropping the superscripts to ease the notation. The other one is treated in the same manner. For the *slave* side of the mortar we obtain

$$\int_{\gamma_n^-} u_n \widehat{\Phi}_i ds = \sum_{j=1}^{N_n+1} U_{j,n} \int_{\gamma_n^-} \Psi_j \widehat{\Phi}_i ds = \sum_{j=1}^{N_n+1} R_{i,j} U_{j,n}, \quad \text{for } i = 1, \dots, N_n - 1, \quad (26)$$

where $R_{i,j} = \int_{\gamma_n^-} \Psi_j \widehat{\Phi}_i ds$. For the *master* side, using the *mortar condition (i)*, we have that

$$\int_{\gamma_n^-} u_m \widehat{\Phi}_i ds = \sum_{j=1}^{N_m+1} U_{j,m} \int_{\gamma_n^-} \Phi_j \widehat{\Phi}_i ds = \sum_{j=1}^{N_m+1} P_{i,j} U_{j,m}, \quad \text{for } i = 1, \dots, N_n - 1, \quad (27)$$

with $P_{i,j} = \int_{\gamma_n^-} \Phi_j \widehat{\Phi}_i ds$. One may use (26)-(27) to recast the mortar constraint **MC1** in matrix notation

$$\underline{R} \begin{bmatrix} U_{1,n} \\ \vdots \\ U_{N_n+1,n} \end{bmatrix} = \underline{P} \begin{bmatrix} U_{1,m} \\ \vdots \\ U_{N_m+1,m} \end{bmatrix}$$

Now, to compute numerically the matrices \underline{R} and \underline{P} we use suitable quadrature formulas depending if we are on the *slave* or in the *master* side of the *mortar*. We choose $N_n + 1$ GLL nodes to evaluate the integrals $\int_{\gamma_n^-} \Psi_j \widehat{\Phi}_i ds$ such that the matrix \underline{R} takes a special structure. In fact, because of this choice the interior part \underline{R}_{int} is diagonal. The first and the last columns are full but they are concerned only with degrees of freedom (namely, $U_{1,n}$ and $U_{N_n+1,n}$) but do not depend on the matching conditions. We observe also that the matrix \underline{P} is full. Then the local projection operator can be written in a matrix form as

$$\begin{bmatrix} U_{2,n} \\ \vdots \\ U_{N_n,n} \end{bmatrix} = \underline{R}_{int}^{-1} \underbrace{\begin{bmatrix} P_{1,1} & \cdots & P_{1,N_m+1} & -R_{1,1} & -R_{1,N_n+1} \\ \vdots & \ddots & \vdots & \vdots & \vdots \\ P_{N_n-1,1} & \cdots & P_{N_n-1,N_m+1} & -R_{N_n-1,1} & -R_{N_n-1,N_n+1} \end{bmatrix}}_{\underline{Q}_n} \begin{bmatrix} U_{1,m} \\ \vdots \\ U_{N_m+1,m} \\ U_{1,n} \\ U_{N_n+1,n} \end{bmatrix}.$$

Thanks to the projection operator \underline{Q}_n , we are then able to recover the *slave* unknowns in γ_n^- once we know the *master* ones. To obtain a global projection operator \widetilde{Q} we proceed as follows. For each component of \mathbf{u} we denote by \mathbf{U}_{slave} the vector of unknowns associated to d.o.f. that lay on the slave side of \mathcal{S} and by \mathbf{U}_{master} the vector of unknowns associated to all the remaining d.o.f. Then, for each γ_n^- belonging to the skeleton \mathcal{S} we build the local projection operator \underline{Q}_n and we store it into the matrix \widetilde{Q} . In this way \widetilde{Q} has a block structure of the form

$$\widetilde{Q} = \begin{bmatrix} \widehat{Q} & \underline{0} \\ \underline{0} & \underline{Q} \end{bmatrix}, \quad (28)$$

where \widehat{Q} is a block diagonal matrix with a block equal to the identity and the other equal to the rectangular matrix \underline{Q} containing all the local matrices \underline{Q}_n . Thus, we have that the global linear system can be expressed as

$$\widetilde{Q}^\top \widetilde{M} \widetilde{Q} \ddot{\mathbf{U}}_{master} + \widetilde{Q}^\top \widetilde{A} \widetilde{Q} \mathbf{U}_{master} = \widetilde{Q}^\top \mathbf{F}^{ext}, \quad (29)$$

where the matrices \widetilde{M} and \widetilde{A} have columns and rows modified with respect to the ones of \underline{M} and \underline{A} according to latter assumptions on the unknowns reordering. All the terms appearing in the matrices of the two algebraic formulation are computed using Gauss-Lobatto quadrature rule in which the quadrature points coincide with the GLL points. We remark that since the term $\Psi_j \Psi_i \in \mathbf{Q}_{N_k}$, for some k , while the Gauss-Lobatto rule with N_k points is exact for polynomials up to degree $2N_k - 1$, the spectral mass matrix \underline{M} are slightly under integrated. However, the final accuracy of spectral methods is maintained [14].

4.1.1 Structural damping

When using equation (5) to model viscoelastic materials, very useful for seismic applications, we must compute additional external forces:

$$\mathbf{F}^{visc} = -\underline{\mathbf{C}}\dot{\mathbf{U}} - \underline{\mathbf{D}}\mathbf{U},$$

or equivalently

$$\begin{bmatrix} \mathbf{F}^{visc,1} \\ \mathbf{F}^{visc,2} \end{bmatrix} = - \begin{bmatrix} \underline{\mathbf{C}}^1 & \underline{\mathbf{0}} \\ \underline{\mathbf{0}} & \underline{\mathbf{C}}^2 \end{bmatrix} \begin{bmatrix} \dot{\mathbf{U}}^1 \\ \dot{\mathbf{U}}^2 \end{bmatrix} - \begin{bmatrix} \underline{\mathbf{D}}^1 & \underline{\mathbf{0}} \\ \underline{\mathbf{0}} & \underline{\mathbf{D}}^2 \end{bmatrix} \begin{bmatrix} \mathbf{U}^1 \\ \mathbf{U}^2 \end{bmatrix},$$

where the matrices $\underline{\mathbf{C}}^\ell$ and $\underline{\mathbf{D}}^\ell$, for $\ell = 1, 2$ are block diagonal. Each block $\underline{\mathbf{C}}_k^\ell$ and $\underline{\mathbf{D}}_k^\ell$ is associated to the spectral element Ω_k and

$$\mathbf{C}_k^\ell(i, j) = (\rho\zeta\Psi_j^\ell, \Psi_i^\ell)_{\Omega_k}, \quad \mathbf{D}_k^\ell(i, j) = (\rho\zeta^2\Psi_j^\ell, \Psi_i^\ell)_{\Omega_k}, \quad (30)$$

respectively for $i, j = a_k, \dots, b_k$. Then the final discretized system becomes:

$$\underline{\mathbf{M}}\ddot{\mathbf{U}} + \underline{\mathbf{C}}\dot{\mathbf{U}} + (\underline{\mathbf{A}} + \underline{\mathbf{B}} + \underline{\mathbf{D}})\mathbf{U} = \mathbf{F}^{ext}, \quad (31)$$

where the accelerations $\ddot{\mathbf{U}}$ and the velocities $\dot{\mathbf{U}}$ are approximated as described in the following section.

4.2 Time integration scheme

Let now subdivide the interval $(0, T]$ into N subinterval of amplitude $\Delta t = T/N$: at every time level $t_n = n\Delta t$, for $n = 0, \dots, N$, the time integration scheme is achieved with the second order Leap-Frog scheme (cf. [40]):

$$\underline{\mathbf{M}}\mathbf{U}(t_{n+1}) = [2\underline{\mathbf{M}} - \Delta t^2(\underline{\mathbf{A}} + \underline{\mathbf{B}})] \mathbf{U}(t_n) - \underline{\mathbf{M}}\mathbf{U}(t_{n-1}) + \Delta t^2\mathbf{F}^{ext}(t_n), \quad (32)$$

or

$$\begin{aligned} \underline{\tilde{\mathbf{Q}}}^\top \underline{\tilde{\mathbf{M}}}\underline{\tilde{\mathbf{Q}}}\mathbf{U}_{master}(t_{n+1}) &= \underline{\tilde{\mathbf{Q}}}^\top [(2\underline{\tilde{\mathbf{M}}} - \Delta t^2\underline{\tilde{\mathbf{A}}})\underline{\tilde{\mathbf{Q}}}\mathbf{U}_{master}(t_n) \\ &\quad - \underline{\tilde{\mathbf{M}}}\underline{\tilde{\mathbf{Q}}}\mathbf{U}_{master}(t_{n-1}) + \Delta t^2\mathbf{F}^{ext}(t_n)], \end{aligned} \quad (33)$$

respectively for (22) and (29), with initial conditions $\mathbf{U}(t_0) = \mathbf{u}_0$ and $\dot{\mathbf{U}}(t_0) = \mathbf{u}_1$. In particular if a DGSEM is employed the iteration matrix $\underline{\mathbf{M}}$ in (32) is diagonal and can be inverted at very low computational cost. In the MSEM the matrix $\underline{\tilde{\mathbf{Q}}}^\top \underline{\tilde{\mathbf{M}}}\underline{\tilde{\mathbf{Q}}}$ is non-diagonal, but taking advantage of the structure of $\underline{\tilde{\mathbf{Q}}}$ it is possible to split the linear system (33) as follows

$$\begin{bmatrix} \underline{\mathbf{M}}_{master} & 0 \\ 0 & \underline{\mathbf{Q}}^\top \underline{\mathbf{M}}_{slave} \underline{\mathbf{Q}} \end{bmatrix} \begin{bmatrix} \mathbf{U}_{master}^{\mathcal{I}}(t_{n+1}) \\ \mathbf{U}_{master}^{\mathcal{S}}(t_{n+1}) \end{bmatrix} = \begin{bmatrix} \mathbf{b}_{master}^{\mathcal{I}} \\ \underline{\mathbf{Q}}^\top \mathbf{b}_{slave}^{\mathcal{S}} \end{bmatrix}, \quad (34)$$

with $\mathbf{b} = [(2\underline{\tilde{\mathbf{M}}} - \Delta t^2\underline{\tilde{\mathbf{A}}})\underline{\tilde{\mathbf{Q}}}\mathbf{U}(t_n) - \underline{\tilde{\mathbf{M}}}\underline{\tilde{\mathbf{Q}}}\mathbf{U}(t_{n-1}) + \Delta t^2\mathbf{F}^{ext}(t_n)]$. Here the superscripts \mathcal{I} and \mathcal{S} identify those unknowns belonging respectively to the interior

or to the skeleton of the domain. Then at each time step we solve separately the two blocks of the linear system (34). In particular for the non-diagonal block we perform the LU-factorization (see [37]).

To ensure stability, the explicit time integration scheme must satisfy the usual Courant-Friedrichs-Levy (CFL) condition (see [38]) that imposes a restriction on Δt . We see in the next section that this limitation is proportional to the minimal distance between two neighbouring spectral nodes of the numerical grid. Since this distance scales as $h_k N_k^{-2}$ (h_k size of the spectral element Ω_k), the stability requirement on Δt may become too restrictive for very large polynomial degrees N_k . For these cases an implicit time scheme is recommended.

5 Analysis of grid dispersion and stability

In this section we study in detail the MSEM and the DGSEM in the two dimensional case, doing the so called Von-Neumann analysis, namely the analysis of grid dispersion and stability. The former criterion determines the largest sampling ratio for the spatial discretization (i.e., the number of nodes per wavelength) such that the numerical solution has a prescribed accuracy. The latter determines the largest time step Δt that we are allowed to use in the explicit time integration scheme, such that the solution remains bounded with respect to problem's data. For the sake of simplicity, we present the dispersion and stability analysis in a two dimensional framework.

To start with, let us consider the wave equation (1) in an isotropic, elastic, unbounded domain Ω , with $\mathbf{u}(\mathbf{x}, t) \rightarrow 0$ for all t as $|\mathbf{x}| \rightarrow \infty$ and $\mathbf{u}_0 = \mathbf{u}_1 = 0$. Finally, we also assume $\mathbf{f} \equiv 0$, this is not a limitation. These are standard assumptions when using the Von Neumann's method (plane wave analysis), see [2, 3, 4, 21, 19, 48, 36, 34].

At the discrete level we assume that Ω is partitioned into non-overlapping spectral elements Ω_k having uniform size h . This partitioning is supposed to be periodic and made by squared elements with sides parallel to the coordinate axes (cf. Figure 6). We also suppose the polynomial approximation degree equals N in each Ω_k .

5.1 Grid dispersion - DGSEM

We report the analysis of grid dispersion for the DGSEM, see also [21] for the scalar case. Let identify by Ψ^{ℓ, Ω_f} , $\ell = 1, 2$ the basis functions with support in Ω_f with $f \in \{C, T, B, L, R\}$ (cf. Figure 6). Without loss of generality, we consider respectively test and trial functions of the following form

$$\Psi_i^\ell = \begin{cases} \Psi_i^{\ell, \Omega_C} & \text{in } \Omega_C, \\ \mathbf{0} & \text{otherwise,} \end{cases} \quad \text{and } \Psi_j^\ell = \begin{cases} \Psi_j^{\ell, \Omega_C} & \text{in } \Omega_C, \\ \Psi_j^{\ell, \Omega_f} & \text{in } \Omega_f, f \in \{T, B, L, R\}, \\ \mathbf{0} & \text{otherwise.} \end{cases} \quad (35)$$

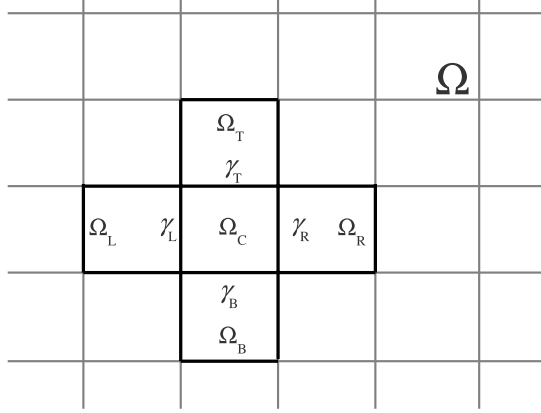


Figure 6: Periodic grid made by squared elements with side parallel to the coordinate axis. The reference element Ω_C with sides γ_f and neighbouring elements Ω_f , for $f = \{R, L, T, B\}$.

By rewriting the equation (21), we obtain a rectangular linear system in the unknowns

$$\mathbf{U}^\ell = [\mathbf{U}^{\ell, \Omega_C}, \mathbf{U}^{\ell, \Omega_T}, \mathbf{U}^{\ell, \Omega_B}, \mathbf{U}^{\ell, \Omega_L}, \mathbf{U}^{\ell, \Omega_R}], \quad \ell = 1, 2. \quad (36)$$

Clearly this system is underdetermined because the number of columns, $10(N+1)^2$, exceeds the number of rows, $2(N+1)^2$. To reduce it into a square linear system we make use of the following plane wave hypothesis.

Let us assume that the displacement is a plane wave, i.e., in Ω_C we have

$$U_j^{\ell, \Omega_C} = c_j^\ell e^{i(\mathbf{k} \cdot \mathbf{p}_j - \omega t)}, \quad \ell = 1, 2, \quad (37)$$

where $\kappa = (k_x, k_y)$ is the wave vector, \mathbf{p}_j contains the j^{th} node in Cartesian coordinates and c_j are arbitrary constants. The above assumption implies that

$$U_j^{\ell, \Omega_f} = e^{\beta_f} U_j^{\ell, \Omega_C}, \quad \ell = 1, 2, \quad (38)$$

with $\beta_f = \{-ik_y h, ik_y h, -ik_x h, ik_x h\}$ and $f = \{T, B, R, L\}$, respectively. Substituting (38) in (36) we obtain the modified square linear system of size $2(N+1)^2$:

$$\begin{bmatrix} \underline{\mathbf{M}}^1 & \underline{\mathbf{0}} \\ \underline{\mathbf{0}} & \underline{\mathbf{M}}^2 \end{bmatrix} \begin{bmatrix} \ddot{\mathbf{U}}^{1, \Omega_C} \\ \ddot{\mathbf{U}}^{2, \Omega_C} \end{bmatrix} + \begin{bmatrix} \underline{\mathbf{A}}^1 + \tilde{\underline{\mathbf{B}}}^1 & \underline{\mathbf{A}}^2 + \tilde{\underline{\mathbf{B}}}^2 \\ \underline{\mathbf{A}}^3 + \tilde{\underline{\mathbf{B}}}^3 & \underline{\mathbf{A}}^4 + \tilde{\underline{\mathbf{B}}}^4 \end{bmatrix} \begin{bmatrix} \mathbf{U}^{1, \Omega_C} \\ \mathbf{U}^{2, \Omega_C} \end{bmatrix} = \begin{bmatrix} \mathbf{0} \\ \mathbf{0} \end{bmatrix}, \quad (39)$$

where $\underline{\mathbf{M}}^i$, $i = 1, 2$, and $\underline{\mathbf{A}}^i$, $i = 1, \dots, 4$, are defined in (23) and (24) respectively. The matrices $\tilde{\underline{\mathbf{B}}}^\ell$, for $\ell = 1, \dots, 4$, are defined taking into account the hypothesis of periodicity of the discretization and the plane wave assumption (37); for example $\tilde{\underline{\mathbf{B}}}^1$ is given by

$$\tilde{\underline{\mathbf{B}}}^1(i, j) = \underline{\mathbf{B}}^1(i, j) + \sum_{f=\{T, B, R, L\}} e^{\beta_f} \underline{\mathbf{B}}^{1, f}(i, j), \quad i, j = 1, \dots, (N+1)^2,$$

where

$$\begin{aligned}\underline{\mathbf{B}}^1(i, j) &= \sum_{f=\{T, B, R, L\}} - \int_{\gamma_f} \{\underline{\sigma}(\Psi_j^{1, \Omega_C})\} : \llbracket \Psi_i^{1, \Omega_C} \rrbracket ds \\ &+ \theta \int_{\gamma_f} \llbracket \Psi_j^{1, \Omega_C} \rrbracket : \{\underline{\sigma}(\Psi_i^{1, \Omega_C})\} ds + \eta_f \int_{\gamma_f} \llbracket \Psi_j^{1, \Omega_C} \rrbracket : \llbracket \Psi_i^{1, \Omega_C} \rrbracket ds,\end{aligned}$$

and

$$\begin{aligned}\underline{\mathbf{B}}^{1, f}(i, j) &= - \int_{\gamma_f} \{\underline{\sigma}(\Psi_j^{1, \Omega_f})\} : \llbracket \Psi_i^{1, \Omega_C} \rrbracket ds + \theta \int_{\gamma_f} \llbracket \Psi_j^{1, \Omega_f} \rrbracket : \{\underline{\sigma}(\Psi_i^{1, \Omega_C})\} ds \\ &+ \eta_f \int_{\gamma_f} \llbracket \Psi_j^{1, \Omega_f} \rrbracket : \llbracket \Psi_i^{1, \Omega_C} \rrbracket ds.\end{aligned}$$

Similarly, we define the elements of the matrices $\tilde{\mathbf{B}}^\ell$ for $\ell = 2, 3, 4$. Now, calculating the second derivative with respect to time of $\mathbf{U}^{\ell, \Omega_C}$ and setting $\tilde{\mathbf{K}} = \underline{\mathbf{A}} + \tilde{\mathbf{B}}$ we obtain the following generalized eigenvalue problem

$$\tilde{\mathbf{K}}\mathbf{U}^{\Omega_C} = \Lambda \underline{\mathbf{M}}\mathbf{U}^{\Omega_C}, \quad (40)$$

where $\Lambda = \omega_h^2$, with ω_h the angular frequency at which the wave travels in the grid. As observed in [20, 21] and in [44] the number of eigenvalues of problem (40) naturally exceeds the number of admissible physical modes. Then we need a strategy to select which eigenvalues correspond to the compressional (c_P) and the shear (c_S) wave velocities. We do this by computing all the velocities associated to the eigenvalues of (40) and then comparing them to the real c_P and c_S velocities defined in (4).

We denote by Λ_P and Λ_S the eigenvalues used to compute the best approximations of c_P and c_S , namely $c_{P, h}$ and $c_{S, h}$.

Note that the system (40) for the NIPG method is not symmetric thus complex eigenvalues are possible. However in [21] it has been remarked that Λ_P and Λ_S are in fact always real numbers. Next we define the grid dispersion of pressure and shear waves as the ratio between the velocity at which the wave travels in the grid (numerical velocity) and the physical velocity. By definition the numerical shear velocity $c_{S, h}$ is given by $c_{S, h} = h\omega_h/(2\pi\delta)$, where $\delta = h/(NL)$ is the sampling ratio (or equivalently δ^{-1} is the number of GLL points per wavelength), and L is the wavelength of the plane wave. We have that $c_{S, h} = h\sqrt{\Lambda_S}/(2\pi\delta)$, and therefore the grid dispersion is the relative error in the velocity, given by $e_S = c_{S, h}/c_S - 1$. Analogously $c_{P, h} = h\sqrt{\Lambda_P}/(2\pi\delta)$ and $e_P = c_{P, h}/c_P - 1$.

5.2 Grid dispersion - MSEM

In order to carry out a dispersion analysis for the MSEM, we adopt a strategy similar to the one described for the DGSEM. The goal is the definition of a generalized eigenvalue problem associated only to the degrees of freedom belonging

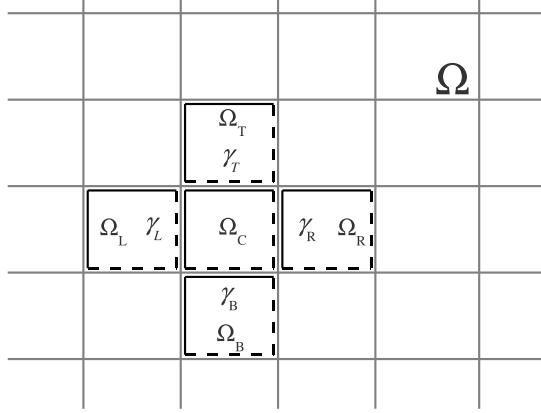


Figure 7: Periodic grid made by squared elements with side parallel to the coordinate axis. The reference element Ω_C with sides γ_f and neighbouring elements Ω_f , for $f = \{R, L, T, B\}$. Solid lines (-) are the *master* edges and dashed lines (- -) are the *slave* edges.

to Ω_C . Under the hypothesis of shape regularity and periodicity of the mesh, we observe that the skeleton of the partitioning is uniquely defined once the *master* and *slave* edges for the reference element Ω_C are selected. Consider the configuration shown in Figure 7: this is the unique, up to a rotation, possible combination of *master* and *slave* edges for Ω_C that does not violate the hypothesis of grid periodicity.

We rewrite the ODE system (21) in the MSEM framework: using (35) we obtain

$$\underline{\mathbf{M}}\ddot{\mathbf{U}}^{\Omega_C} + \underline{\mathbf{A}}\mathbf{U}^{\Omega_C} = \mathbf{0}, \quad (41)$$

where $\underline{\mathbf{M}}$ and $\underline{\mathbf{A}}$ are defined in (23) and (24), respectively. Next, we impose the *mortar conditions* **MC1** concerning the *slave* unknowns at the interfaces γ_B and γ_R . In particular, for $\ell = 1, 2$ and $f = \{R, B\}$, we have that

$$\sum_{j:\mathbf{p}_j \in \gamma_f} U_j^{\ell, \Omega_C} \int_{\gamma_f} \Psi_j^{\ell, \Omega_C} \widehat{\Phi}_i^\ell ds = \sum_{j:\mathbf{p}_j \in \gamma_f} U_j^{\ell, \Omega_f} \int_{\gamma_f} \Psi_j^{\ell, \Omega_f} \widehat{\Phi}_i^\ell ds \quad \forall \widehat{\Phi}_i^\ell \in \widehat{\Lambda}_\delta(\gamma_f). \quad (42)$$

To recast these conditions in terms of unknowns and basis functions defined only on Ω_C we simply notice that, by periodicity,

$$\Psi_j^{\ell, \Omega_R} \Big|_{\gamma_R} = \Psi_j^{\ell, \Omega_C} \Big|_{\gamma_L} \quad \text{and} \quad \Psi_j^{\ell, \Omega_B} \Big|_{\gamma_B} = \Psi_j^{\ell, \Omega_C} \Big|_{\gamma_T}, \quad \ell = 1, 2 \quad (43)$$

and by the plane wave assumption, equation (38) holds. Substituting (43) in (42) we obtain

$$\sum_{j:\mathbf{p}_j \in \gamma_f} U_j^{\ell, \Omega_C} \int_{\gamma_f} \Psi_j^{\ell, \Omega_C} \widehat{\Phi}_i^\ell ds = \sum_{j:\mathbf{p}_j \in \gamma_f} e^{\beta_f} U_j^{\ell, \Omega_C} \int_{\gamma_f} \Psi_j^{\ell, \Omega_f} \widehat{\Phi}_i^\ell ds \quad \forall \widehat{\Phi}_i^\ell \in \widehat{\Lambda}_\delta(\gamma_f), \quad (44)$$

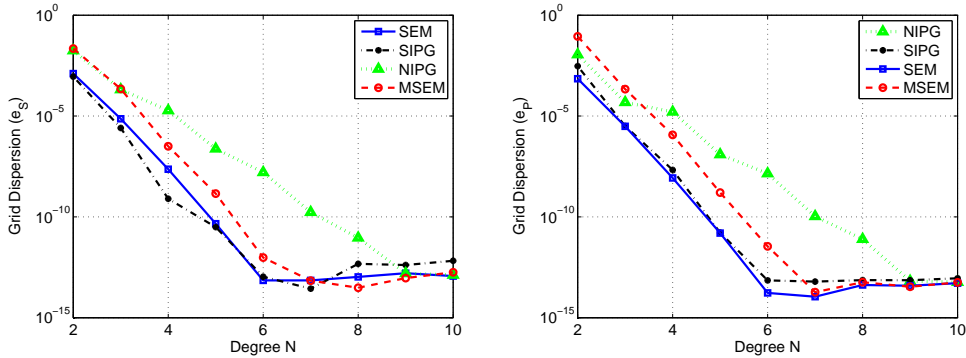


Figure 8: Grid dispersion versus the polynomial degree N : $\delta = 0.2$ and incident angle $\theta = \pi/4$.

for $\ell = 1, 2$ and $f = \{B, R\}$. We remark that the equation (44) relates *slave* unknowns in Ω_C with *master* unknowns still in Ω_C : this means that the matrix projection $\underline{\tilde{Q}}$ refers only to the reference element Ω_C . We use this matrix to reduce the linear system in (41) to one for the *master* unknowns only

$$\underline{\tilde{Q}}^\top \underline{\tilde{M}} \underline{\tilde{Q}} \ddot{\mathbf{U}}_{master}^{\Omega_C} + \underline{\tilde{Q}}^\top \underline{\tilde{A}} \underline{\tilde{Q}} \mathbf{U}_{master}^{\Omega_C} = \mathbf{0}. \quad (45)$$

We notice that $\underline{\tilde{Q}}$ has always a block diagonal structure like (28) where each block $\hat{\underline{Q}}$ is modified according to (44). Calculating the second derivative of the displacement with respect to time and defining $\underline{\tilde{K}} = \underline{\tilde{Q}}^\top \underline{\tilde{A}} \underline{\tilde{Q}}$, we finally obtain the generalized eigenvalue problem of size $2(N^2 + 3)$

$$\underline{\tilde{K}} \mathbf{U}_{master}^{\Omega_C} = \Lambda \underline{\tilde{Q}}^\top \underline{\tilde{M}} \underline{\tilde{Q}} \mathbf{U}_{master}^{\Omega_C}, \quad (46)$$

where $\Lambda = \omega_h^2$ as in the DGSEM case.

We remark that in the definition of e_S and e_P the sign of the error indicates if the numerical approximation causes a delay or an acceleration of the travelling waves. The grid dispersion error will depend on the sampling ratio δ , the wave vector κ , the degree of the basis function N and on the velocities c_P and c_S . For the DGSEM, on the stability parameter η too.

5.3 Grid dispersion - Numerical Results

Now, we analyse the grid dispersion error for both the MSEM and the DGSEM from three different points of view: (i) the convergence with respect to the polynomial degree N , (ii) the convergence with respect to the sampling ratio δ and (iii) the numerical anisotropy introduced by the grid dispersion. Finally we compare the results with the conforming SEM: in this case the grid dispersion analysis is obtained using a technique similar to the one employed in the MSEM and the results obtained are in agreement with [21, 45].

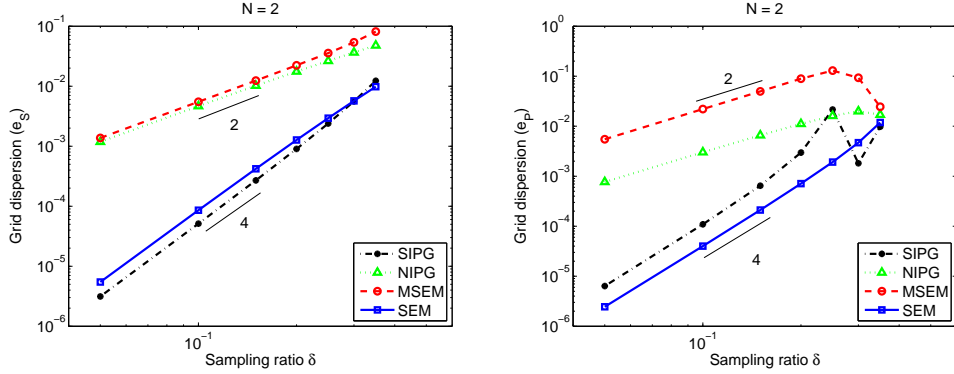


Figure 9: Grid dispersion versus the sampling ratio δ : $N = 2$.

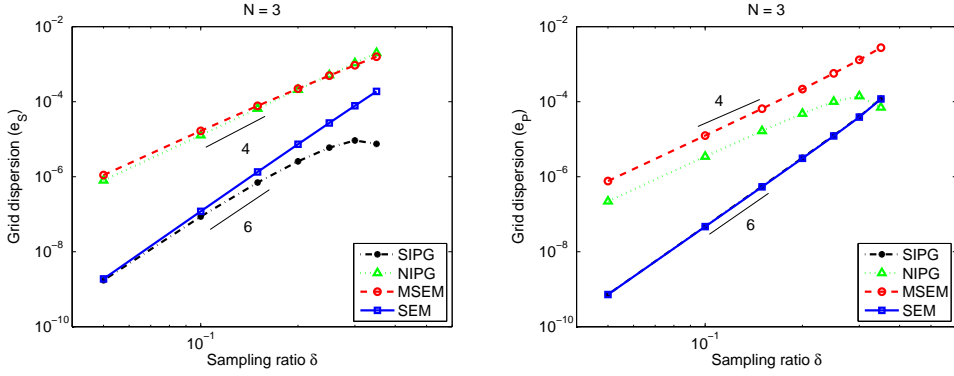


Figure 10: Grid dispersion versus the sampling ratio δ : $N = 3$.

In the first set of experiments, we fix the ratio between the velocities $r = c_P/c_S = 2$ (that is a very common choice in geophysical applications), the incidence angle $\theta = \pi/4$ and, for the DGSEM, we fix the parameter $\eta = 2N^2/h$.

In Figure 8 we show the grid dispersion errors with respect to the degree N of the basis functions, fixing $\delta = 0.2$ (namely 5 grid points per wavelength). All the non-conforming approaches reproduce the same spectral convergence of the SEM. The SIPG and the MSEM reach the threshold value $\approx 10^{-13}$ for $N = 6$ while the NIPG for $N = 9$.

The grid dispersion as a function of sampling ratio δ is shown in Figures 9-12 for the degrees $N = 2, \dots, 5$, respectively. The aim of this analysis is to establish a relation between the absolute value $|e_S|$, resp. $|e_P|$, and the mesh size h (i.e., determine q , resp. q' , such that $|e_S| = \mathcal{O}(h^q)$, resp. $|e_P| = \mathcal{O}(h^{q'})$). The order of convergence is estimated by the slope of these lines in Figures 9-12.

From the results reported in Figures 9-12 it seems that the SIPG converges with order $q = q' = \mathcal{O}(2N)$, as the SEM; whereas a suboptimal order $q = q' =$

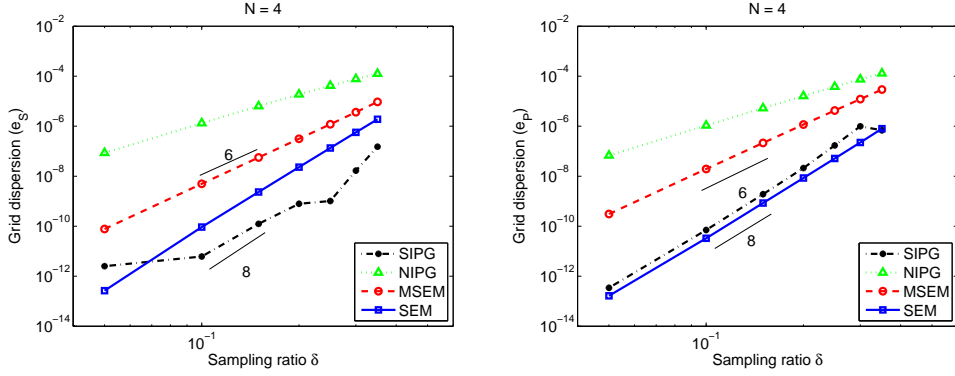


Figure 11: Grid dispersion versus the sampling ratio δ : $N = 4$.

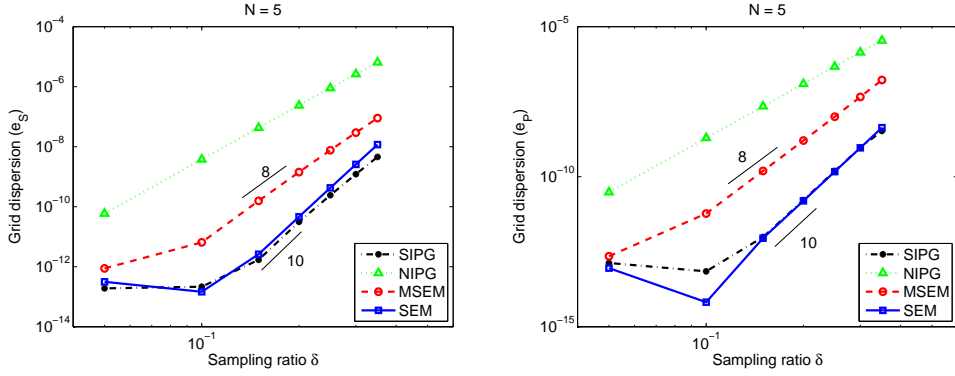


Figure 12: Grid dispersion versus the sampling ratio δ : $N = 5$.

$\mathcal{O}(N + 1)$ is observed for both NIPG and MSE methods. These results are in agreement with [5].

Finally, in Figures 13-16, we show the anisotropy (that is the ratio $c_{S,h}/c_S$ and the ratio $c_{P,h}/c_P$) introduced by the numerical schemes. We consider $N = 2, 3, 4$ and five points per wavelength. For $N > 4$ the anisotropy is very small for all the practical purposes. We notice that, for $N = 2$, in the SIPG and in the MSEM the waves are slightly delayed for all possible incident angles while in the NIPG the waves are accelerated. In Tables 1-2 we also report the maximum value $\max_{1 < \theta < 2\pi} |e_S|$ and $\max_{1 < \theta < 2\pi} |e_P|$ respectively. From these results it can be inferred that all the methods perform in a very similar way.

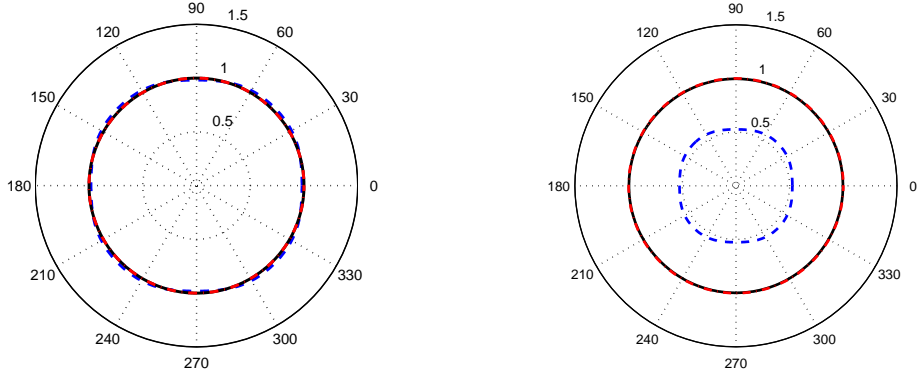


Figure 13: Anisotropy curves $c_{S,h}/c_S$ of the SEM (left) and MSEM (right): sampling ratio $\delta = 0.2$ for polynomial degrees $N = 2$ (- -), $N = 3$ (-) and $N = 4$ (-.). For visualization purposes, the grid dispersion has been magnified by a factor 20.

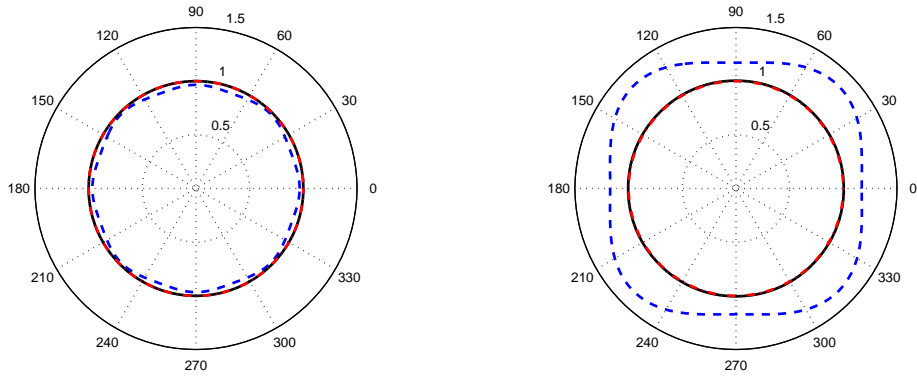


Figure 14: Anisotropy curves $c_{S,h}/c_S$ of the SIPG (left) and NIPG (right): sampling ratio $\delta = 0.2$ for polynomial degrees $N = 2$ (- -), $N = 3$ (-) and $N = 4$ (-.). For visualization purposes, the grid dispersion has been magnified by a factor 20.

N	SEM	SIPG	NIPG	MSEM
2	1.2684e-03	2.7156e-03	1.7540e-02	2.3728e-02
3	8.7429e-06	7.5949e-06	2.7196e-04	2.2247e-04
4	4.2894e-08	5.2818e-08	2.4372e-05	1.3029e-06

Table 1: Maximum value $\max_{0 \leq \theta \leq 2\pi} |e_S|$ for $N = 2, 3, 4$.

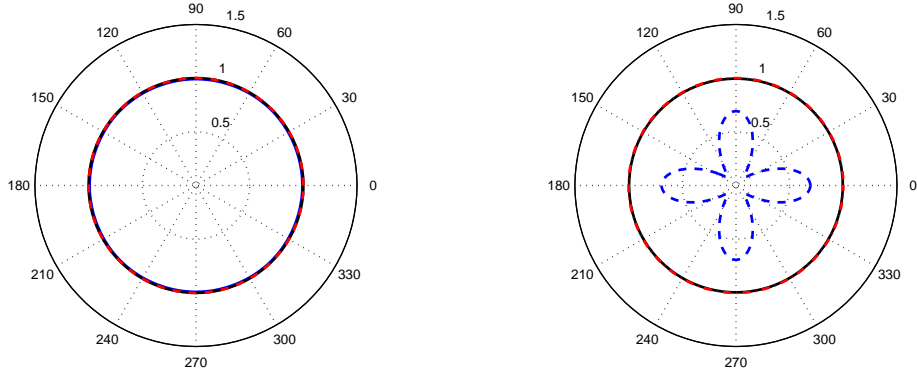


Figure 15: Anisotropy curves $c_{P,h}/c_P$ of the SEM (left) and MSEM (right): sampling ratio $\delta = 0.2$ for polynomial degrees $N = 2$ (- -), $N = 3$ (-) and $N = 4$ (-.). For visualization purposes, the grid dispersion has been magnified by a factor 10.

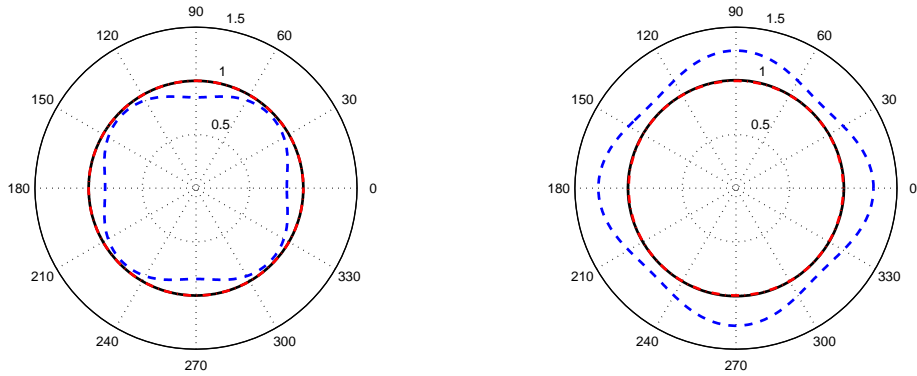


Figure 16: Anisotropy curves $c_{P,h}/c_P$ of the SIPG (left) and NIPG (right): sampling ratio $\delta = 0.2$ for polynomial degrees $N = 2$ (- -), $N = 3$ (-) and $N = 4$ (-.). For visualization purposes, the grid dispersion has been magnified by a factor 10.

N	SEM	SIPG	NIPG	MSEM
2	9.8805e-04	1.5402e-02	2.8146e-02	8.8991e-02
3	6.8628e-06	1.8732e-05	5.6250e-04	2.4218e-04
4	3.1687e-08	3.3492e-07	6.8619e-05	1.5325e-06

Table 2: Maximum value $\max_{0 \leq \theta \leq 2\pi} |e_P|$ for $N = 2, 3, 4$.

5.4 Stability - DGSEM and MSEM

To derive the stability condition for the methods in question we start considering the problem

$$\widehat{\mathbf{M}}\ddot{\mathbf{U}} + \widehat{\mathbf{K}}\mathbf{U} = \mathbf{0}, \quad (47)$$

where all the terms appearing in the above equation are defined on the reference element Ω_C (we omit the superscripts to ease the notation). In the DG framework the matrices $\widehat{\mathbf{K}}$ and $\widehat{\mathbf{M}}$ are $\underline{\mathbf{A}} + \underline{\mathbf{B}}$ and $\underline{\mathbf{M}}$ respectively, while in the *mortar* approach they are equal to $\widetilde{\mathbf{Q}}^\top \underline{\mathbf{A}} \widetilde{\mathbf{Q}}$ and $\widetilde{\mathbf{Q}}^\top \underline{\mathbf{M}} \widetilde{\mathbf{Q}}$ respectively. Assuming that the solution is the plane wave given in (37), substituting this expression in (47) and approximating the second order derivative in time with the Leap-Frog scheme (32) or (33), we obtain the following eigenvalue problem

$$\widehat{\mathbf{K}}\mathbf{U} = \Lambda \widehat{\mathbf{M}}\mathbf{U}, \quad (48)$$

depending on the degrees of freedom inside the reference element Ω_C and where

$$\Lambda = \frac{4}{\Delta t^2} \sin^2 \left(\frac{\omega_h \Delta t}{2} \right).$$

In order to make explicit the dependence of Λ on both the mesh size h and the polynomial approximation degree N we rewrite (48) on $\widehat{\Omega} = (-1, 1)^2$. Collecting out the size of the elements it yields to

$$\widehat{\mathbf{K}}\mathbf{U} = \Lambda' \widehat{\mathbf{M}}\mathbf{U}, \quad (49)$$

with $\Lambda' = (h/\Delta t)^2 \sin^2(\omega_h \Delta t/2)$. Defining the *stability parameter* $q = c_P \Delta t/h$, we deduce the relation

$$q^2 \Lambda' = c_P^2 \sin^2 \left(\frac{\omega_h \Delta t}{2} \right) \leq c_P^2,$$

or equivalently

$$q \leq c_P \frac{1}{\sqrt{\Lambda'}} = c_{cfl}(\Lambda'), \quad (50)$$

As noted in [20], c_{cfl} is a function of Λ' and then depends implicitly on the wave vector κ through the matrices $\widehat{\mathbf{K}}$ and $\widehat{\mathbf{M}}$. Moreover, inequality (50) must be fulfilled for all the eigenvalues and all the wave vectors $\kappa = 2\pi\delta/h(\cos(\theta), \sin(\theta))$. Thus, the stability condition is given by

$$q = \min_{1 \leq j \leq \nu} \min_{0 \leq \theta \leq 2\pi} c_{cfl}(\Lambda'_j(\theta)), \quad (51)$$

where θ is the incident angle of the plane wave and ν is the number of the eigenvalues of problem (49). We remark that condition (51) is equivalent to requiring that

$$q \leq \frac{c(\lambda, \mu)}{\sqrt{\Lambda_{\max}}},$$

where Λ_{\max} is the largest eigenvalue of problem (49) and $c(\lambda, \mu)$ is a positive constant. Thus, by estimating Λ_{\max} in terms of h and N , it is possible to determine a bound for q .

In the DG approach, the bilinear form $\widehat{\mathcal{K}}(\cdot, \cdot)$ associated to the matrix $\widehat{\mathbf{K}}$ in (48) takes the form

$$\begin{aligned} \widehat{\mathcal{K}}(\mathbf{u}, \mathbf{v}) &= \int_{\Omega_C} \underline{\boldsymbol{\sigma}}(\mathbf{u}) : \underline{\boldsymbol{\varepsilon}}(\mathbf{v}) \, d\Omega_1 - \sum_{f=\{T,B,R,L\}} \int_{\gamma_f} \underline{\boldsymbol{\sigma}}(\mathbf{u}) : \mathbf{v} \otimes \mathbf{n} \, ds \\ &\quad + \theta \int_{\gamma_f} (\mathbf{u} - \mathbf{g}_f) \otimes \mathbf{n} : \underline{\boldsymbol{\sigma}}(\mathbf{v}) \, ds + \eta_f \int_{\gamma_f} (\mathbf{u} - \mathbf{g}_f) \otimes \mathbf{n} : \mathbf{v} \otimes \mathbf{n} \, ds, \end{aligned}$$

where the functions $\mathbf{u}, \mathbf{v} \in V_\delta^{DG}$ are zero outside Ω_C , and \mathbf{n} is the normal unit vector pointing outside Ω_C . According to the plane wave hypothesis made at the beginning of Section 5, we take

$$\mathbf{g}_f = e^{\beta_f} \mathbf{u}, \quad \text{for } f = \{T, B, L, R\}.$$

Following [6], it is easy to prove that

$$\widehat{\mathcal{K}}(\mathbf{u}, \mathbf{u}) \leq c(\lambda, \mu, \alpha) \frac{N^4}{h^2} \|\mathbf{u}\|_{L^2(\Omega_C)}^2.$$

Thus, for the generalized eigenvalue problem (49), we can derive the estimate

$$\Lambda_{\max} \leq c(\lambda, \mu, \alpha) \frac{N^4}{h^2},$$

and consequently

$$\Lambda'_{\max} \leq c(\lambda, \mu, \alpha) N^4. \quad (52)$$

For the MSEM we observe that writing Λ'_{\max} by the generalized Rayleigh quotient yields

$$\begin{aligned} \Lambda'_{\max} &= \sup_{\mathbf{v} \in \mathbb{R}^{2m} \setminus \{\mathbf{0}\}} \frac{(\widehat{\mathbf{K}}\mathbf{v}, \mathbf{v})_{\Omega_C}}{(\widehat{\mathbf{M}}\mathbf{v}, \mathbf{v})_{\Omega_C}} = \sup_{\mathbf{v} \in \mathbb{R}^{2m} \setminus \{\mathbf{0}\}} \frac{(\widetilde{\mathbf{Q}}^\top \widetilde{\mathbf{A}} \widetilde{\mathbf{Q}}\mathbf{v}, \mathbf{v})_{\Omega_C}}{(\widetilde{\mathbf{Q}}^\top \widetilde{\mathbf{M}} \widetilde{\mathbf{Q}}\mathbf{v}, \mathbf{v})_{\Omega_C}} \\ &= \sup_{\mathbf{v} \in \mathbb{R}^{2m} \setminus \{\mathbf{0}\}} \frac{(\widetilde{\mathbf{A}} \widetilde{\mathbf{Q}}\mathbf{v}, \widetilde{\mathbf{Q}}\mathbf{v})_{\Omega_C}}{(\widetilde{\mathbf{M}} \widetilde{\mathbf{Q}}\mathbf{v}, \widetilde{\mathbf{Q}}\mathbf{v})_{\Omega_C}} = \sup_{\substack{\mathbf{w} = \widetilde{\mathbf{Q}}\mathbf{v} \in \mathbb{R}^{2n} \setminus \{\mathbf{0}\} \\ \exists i=1, \dots, 2m: \mathbf{v} \cdot \mathbf{e}_i \neq \mathbf{0}}} \frac{(\widetilde{\mathbf{A}}\mathbf{w}, \mathbf{w})_{\Omega_C}}{(\widetilde{\mathbf{M}}\mathbf{w}, \mathbf{w})_{\Omega_C}} \\ &\leq \sup_{\mathbf{v} \in \mathbb{R}^{2n} \setminus \{\mathbf{0}\}} \frac{(\widetilde{\mathbf{A}}\mathbf{v}, \mathbf{v})_{\Omega_C}}{(\widetilde{\mathbf{M}}\mathbf{v}, \mathbf{v})_{\Omega_C}} = \sup_{\mathbf{v} \in \mathbb{R}^{2n} \setminus \{\mathbf{0}\}} \frac{(\underline{\mathbf{A}}\mathbf{v}, \mathbf{v})_{\Omega_C}}{(\underline{\mathbf{M}}\mathbf{v}, \mathbf{v})_{\Omega_C}}, \end{aligned} \quad (53)$$

where $m = (N^2 + 3)$ and $n = (N + 1)^2$. In this way we obtain an upper bound for the maximum eigenvalue of (49) when using MSEM approximation. In fact the

N	SEM	MSEM	SIPG	NIPG
2	0.3376	0.3333	0.2621	0.2163
3	0.1967	0.1770	0.1368	0.1045
4	0.1206	0.1118	0.0795	0.0607
5	0.0827	0.0776	0.0530	0.0400
6	0.0596	0.0570	0.0374	0.0281
7	0.0449	0.0434	0.0280	0.0210
8	0.0351	0.0342	0.0216	0.0162
9	0.0281	0.0277	0.0172	0.0129
10	0.0231	0.0227	0.0140	0.0105
N -rate	-1.8463	-1.8253	-1.9247	-1.9360

Table 3: Computed upper bound for the stability parameter q using $r = 1.414$: rate of decay with respect to N .

last term in (53) is exactly the maximum eigenvalue of the SEM discretization for which the following estimate holds (cf. [11])

$$c_1 N^4 \leq \Lambda'_{\max} \leq c_2 N^4,$$

for c_1 and c_2 positive constants. We remark that in agreement with [6], we notice that for $d = 2$ the estimate (52) does not depend on h . This behaviour is confirmed from the results in Table 3. Finally, we can resume the stability analysis in the following statement.

Proposition 5.1 *For every $\mu > 0$, $\lambda \geq 0$ and $\alpha \geq \alpha_{\min} > 0$, the CFL condition (50) is satisfied for both MSEM and DGSEM if there exists a positive constant $c^*(\lambda, \mu, \alpha)$ such that*

$$q \leq \frac{c^*(\lambda, \mu, \alpha)}{N^2}. \quad (54)$$

Moreover for the MSEM and the NIPG it holds $\alpha_{\min} = 0$ and $c^*(\lambda, \mu, \alpha) = c^*(\lambda, \mu)$.

We remark that for the SIPG, the constant $c^*(\lambda, \mu, \alpha)$ is proportional to $\alpha^{-1/2}$ (cf. [6]), then a less restrictive bound for q in (54) is achieved when $\alpha = \alpha_{\min}$. Moreover it is possible to determine exactly the threshold value α_{\min} (cf. [25] for the elliptic case), but this is not the objective of this study. For the following numerical simulations we choose $\alpha = 1$.

5.5 Stability - Numerical Results

To determine an upper bound for the stability parameter q we fix $\delta = 0.2$ and the ratio $r = 1.414$. This choice gives a more restrictive stability condition: higher values of $r = c_P/c_S$ produce milder stability condition [20]. As for the grid dispersion analysis we have fixed $\eta = 2N^2/h$ for the SIPG and the NIPG methods. In Table 3 are shown the estimated threshold values for q , for $N =$

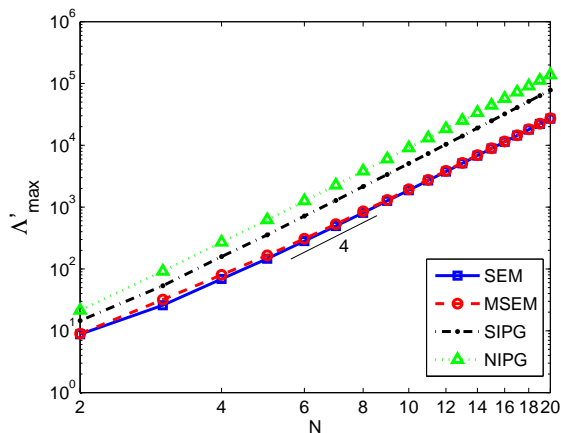


Figure 17: Λ'_{\max} versus the polynomial degree N for the generalized eigenvalue problem (49).

N	SEM	MSEM	SIPG	NIPG
2	0.6752	0.6667	0.5241	0.4326
3	0.7115	0.6403	0.4951	0.3782
4	0.6983	0.6474	0.4607	0.3516
5	0.7039	0.6608	0.4515	0.3409
6	0.7017	0.6712	0.4400	0.3315
7	0.7009	0.6769	0.4360	0.3273
8	0.7005	0.6819	0.4303	0.3228
9	0.6994	0.6878	0.4282	0.3206
10	0.6995	0.6871	0.4247	0.3180

Table 4: Computed upper bound for the stability parameter q' using $r = 1.414$. Note that q' is proportional to qN^2 thus constant for different choices of Δx .

2, ..., 10. The constants for the SIPG are around 70 percent with respect the SEM, while for the MSEM are around 95 percent. The NIPG has constants always more restrictive than those of SIPG.

In Table 3 it is also shown the asymptotic behaviour of the c_{cfl} with respect to N (N -rate): as expected the decay rate of q is approximately proportional to N^{-2} . We remark that the N -rate is computed using polynomial degree up to 20. In Figure 17 we show the trend of Λ'_{\max} with respect to the polynomial degree, in agreement with the theoretical estimate. In practice, the time step is often bounded, not by the size of the spectral elements h , but by the smaller space increment Δx , then, in Table 4 we compute the upper bounds for the modified stability parameter $q' = c_P \Delta t / \Delta x$. It is evident that the CFL condition (51) is less restrictive for the MSEM than for the DGSEM. Then the MSEM allows for larger time step Δt in the explicit time integration scheme.

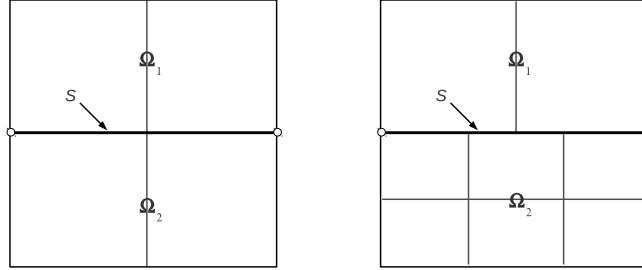


Figure 18: First level of refinement (L1) for the grid A (left) and B (right). The end points of the skeleton \mathcal{S} are highlighted by two circles.

6 Accuracy and order of convergence

Firstly we discuss the accuracy of the MSEM and of the DGSEM on a test case where the exact solution is known. We analyse a wave propagation problem in $\Omega = (0, 1)^2$, setting the elastic parameters $\lambda = \mu = \rho = 1$, and choosing \mathbf{f} such that the exact solution of (1) is

$$\mathbf{u}(t, x, y) = \sin(\sqrt{2}\pi t) \begin{bmatrix} -\sin^2(\pi x) \sin(2\pi y) \\ \sin(2\pi x) \sin^2(\pi y) \end{bmatrix}. \quad (55)$$

The Dirichlet boundary conditions on $\partial\Omega$ and the initial displacement \mathbf{u}_0 and initial velocity \mathbf{u}_1 are set accordingly.

We then subdivide Ω into two subregions Ω_1 and Ω_2 with partitioning \mathcal{T}_{h_1} and \mathcal{T}_{h_2} and fix N_1 and N_2 as the degree of the spectral expansion in each subregion respectively. The skeleton is defined by $\mathcal{S} = \partial\bar{\Omega}_1 \cap \partial\bar{\Omega}_2$ as it is shown in Figure 18. In order to study the property of convergence of MSEM and DGSEM with respect to $\mathbf{h} = (h_1, h_2)$ and $\mathbf{N} = (N_1, N_2)$ we examine two different situations: the first corresponding to a Cartesian matching grid (Figure 18, left) while the second to a Cartesian non-matching grid (Figure 18, right), referred to as **grid A** and **grid B**, respectively. In Figure 18 is shown the first level (L1) of refinement for both grids, corresponding to the initial mesh sizes h_1 and h_2 for Ω_1 and Ω_2 . At each further step of refinement (for a maximum number of four steps), we consider a uniform refinement of the grids at the previous level, in particular for **grid A**, L_i refers to $h_1 = h_2 = 2^{-i}$ whereas for **grid B**, L_i refers to $h_1 = 2^{-i}$ and $h_2 \approx (2/3)h_1$. For the time integration we employ the second order explicit Leap-Frog scheme described in Section 4.

For SEM approximations we recall that, under suitable assumptions on the partition size \mathbf{h} and on the polynomial degree \mathbf{N} an a priori error bound of the

following form holds (see [15])

$$\|\mathbf{u} - \mathbf{u}_\delta\|_{L^2(\Omega)} \leq C \left[\Delta t^2 + \left(\sum_{k=1}^K \overline{C}(s_k) h_k^{2r_k} N_k^{-2s_k} \|\mathbf{u}\|_{H^{s_k}(\Omega_k)}^2 \right)^{\frac{1}{2}} \right],$$

for C and \overline{C} positive constants. Here s_k represents the Sobolev regularity of \mathbf{u} in Ω_k , $r_k = \min(N_k + 1, s_k)$ and Δt the time step.

In particular, if the mesh size \mathbf{h} is constant (i.e., $h_1 = \dots = h_K = h$) we expect exponential convergence in $N = \min_k N_k$, whereas if the spectral order of approximation \mathbf{N} is fixed (i.e., $N_1 = \dots = N_K = N$) we expect algebraic convergence in $h = \max_k h_k$.

In the family of proposed DGSEMs, we analyse in detail the SIPG method (i.e., $\theta = -1$ in (18)) because it exhibits better performances in term of grid dispersion and stability (see Section 5).

In Figure 19 (resp. Figure 21) we report the L^2 -error using MSEM and SIPG with **grid A** for different choices of \mathbf{N} (resp. d.o.f.). The estimated norm is computed at the time $t^* = 2$ using $\Delta t = 5 \cdot 10^{-4}$. All plots in Figures 19-22 are displayed in semilogarithmic scale.

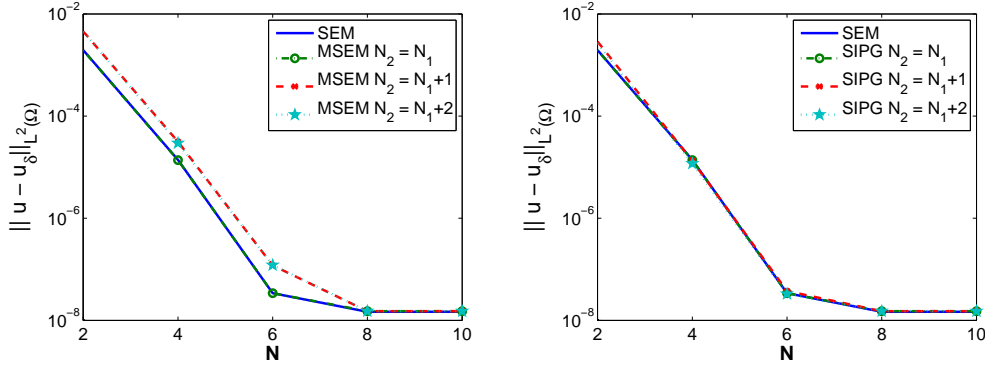


Figure 19: Computed errors versus the polynomial degree N : MSEM (left) and DGSEM (right) at the observation time $t^* = 2$ using $\Delta t = 5 \cdot 10^{-4}$. The results are obtained with the **grid A** and the refinement level L2.

The results show that both methods have the same rate of convergence as the SEM one. In Figure 20 (resp. Figure 22) it is shown the L^2 -error using a different time step $\Delta t = 10^{-4}$ for different choices of \mathbf{N} (resp. d.o.f.).

The results confirm that MSEM and SIPG have both exponential convergence in N , until the threshold value given by $\approx \Delta t^2$ is reached.

Now, we fix $N_1 = N_2$ and we study the accuracy of the two methods with respect to the mesh size h . For each level of refinement we compute the error in L^2 -norm obtained using **grid A** and **grid B**. The algebraic order of convergence $\mathcal{O}(h^{N+1})$ is achieved in both cases for different choices of \mathbf{N} and Δt (see Figures 23-24).

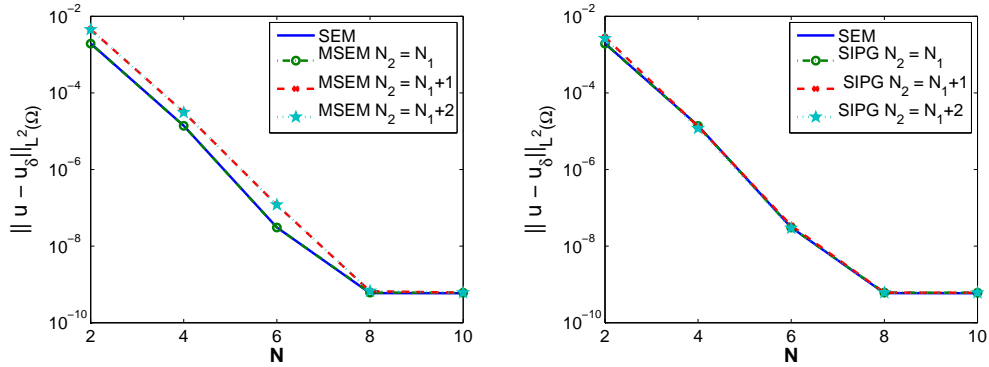


Figure 20: As in Figure 19 with $\Delta t = 10^{-4}$.

Figure 21: Computed errors versus the number of dof: MSEM (left) and DGSEM (right) at the observation time $t^* = 2$ using $\Delta t = 5 \cdot 10^{-4}$. The results are obtained with the grid A and the refinement level L2.

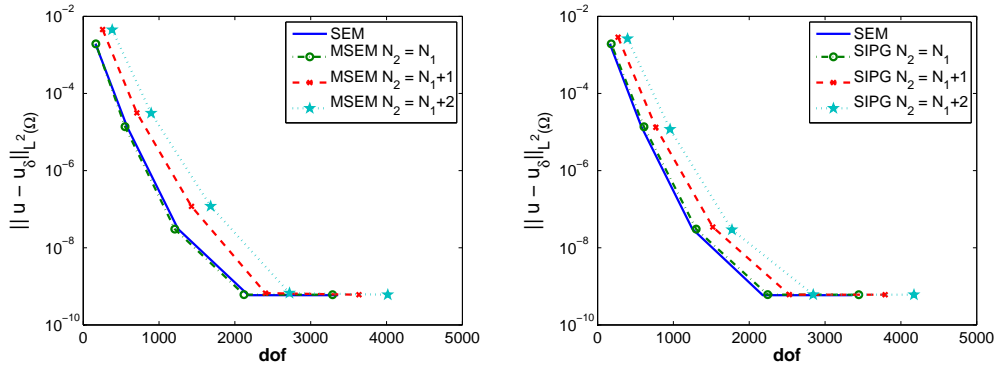


Figure 22: As in Figure 21 with $\Delta t = 10^{-4}$.

Finally in Figure 25 and Figure 26 we show a qualitative analysis of stability of MSEM and SIPG applied to this test case. The results are in agreement with those obtained in Section 5 and confirm that the region of stability for MSEM is larger than that for SIPG. Then, for explicit time integration scheme, MSEM is preferable to SIPG.

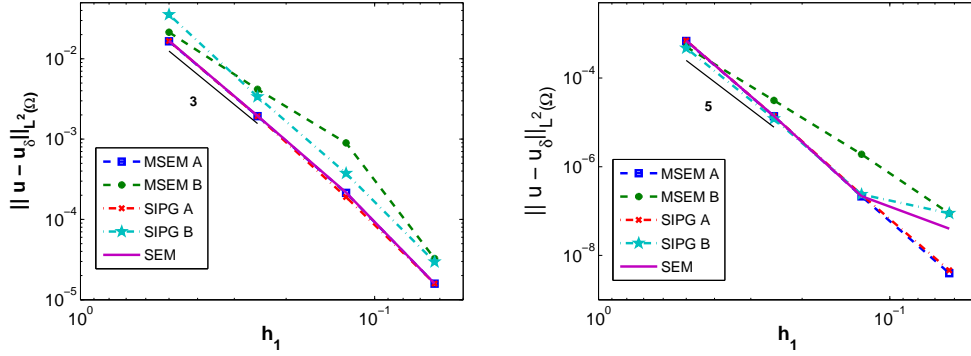


Figure 23: Computed errors versus the mesh size: $N_1 = N_2 = 2$, $\Delta t = 10^{-3}$ (left) and $N_1 = N_2 = 4$ and $\Delta t = 10^{-4}$ (right). The error in the L^2 -norm is computed at the observation time $t^* = 2$ for all the refinement levels L1-L4. The suffixes A,B in the legend refer to the grids employed in the computation.

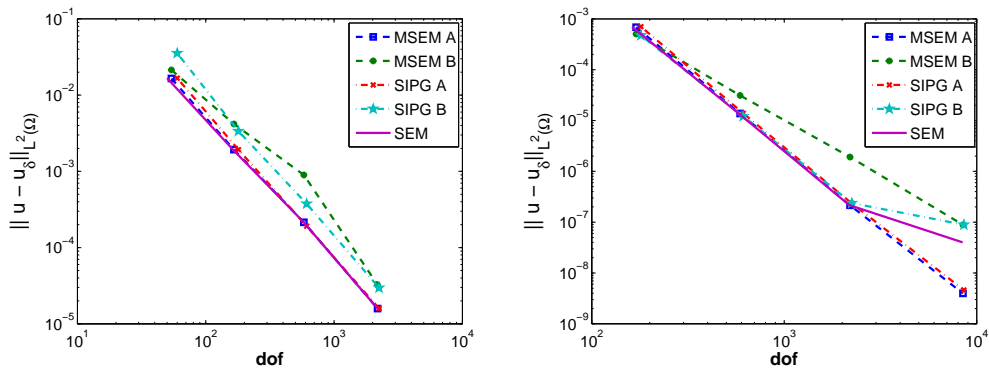


Figure 24: Computed errors versus the mesh size: $N_1 = N_2 = 2$, $\Delta t = 10^{-3}$ (left) and $N_1 = N_2 = 4$ and $\Delta t = 10^{-4}$ (right). The error in the L^2 -norm is computed at the observation time $t^* = 2$ for all the refinement levels L1-L4. The suffixes A,B in the legend refer to the grids employed in the computation.

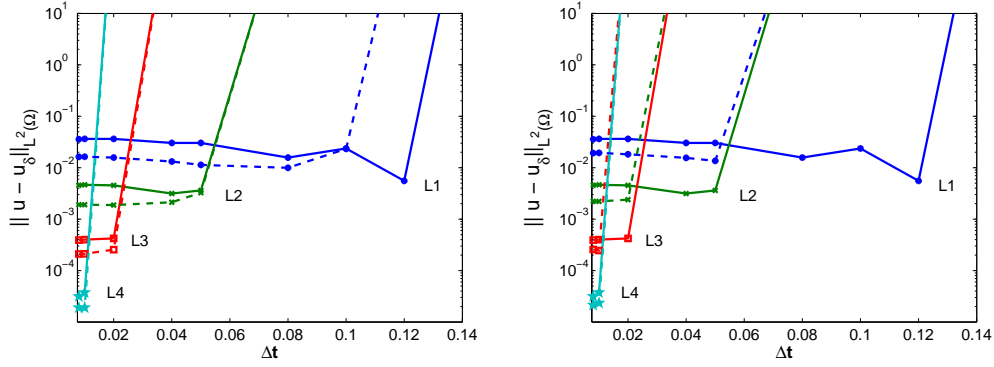


Figure 25: Stability analysis of MSEM (left) and SIPG (right) with respect to the mesh size h . The L^2 -error is computed at the observation time $t^* = 20$ with $N_1 = N_2 = 2$. Solid lines (-) correspond to SEM approximations, while dashed lines (- -) to non-conforming approximations: MSEM on the left and SIPG on the right.

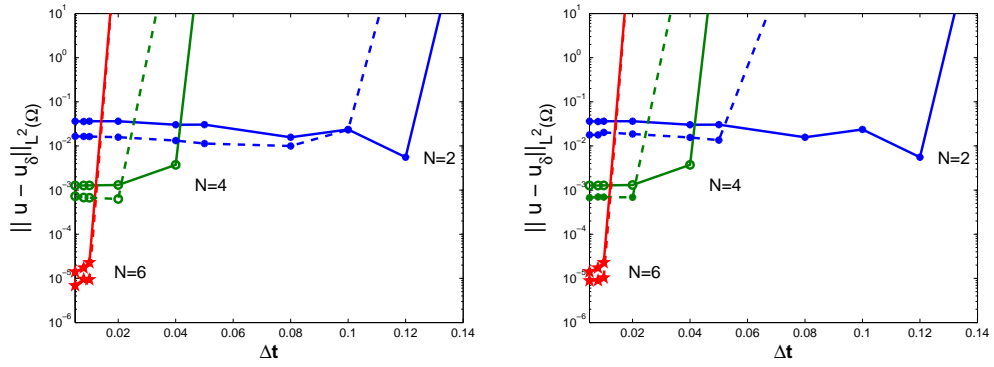


Figure 26: Stability analysis of MSEM (left) and SIPG (right) with respect to the polynomial order N . The L^2 -error is computed at the observation time $t^* = 20$ for the refinement level L1 using the `grid A`. Solid lines (-) correspond to SEM approximations, while dashed lines (- -) to non-conforming approximations: MSEM on the left and SIPG on the right.

7 An application of geophysical interest

In this section we analyze the seismic response of an alluvial basin. We consider the viscoelastic model (5) in the computational domain $(x, z) \in \Omega = (0, 2 \cdot 10^4 m) \times (-9.6 \cdot 10^2 m, f(x))$ where f describes the top profile of the valley, see Figure 27. The bottom and the lateral boundaries are set far enough from the point source so to avoid any interference of possible reflections from non-perfectly absorbing boundaries with the waves of interest that are reflected, transmitted, or converted at the material or free surfaces. We simulate a point source load of the form

$$\mathbf{f}(\mathbf{x}, t) = \mathbf{g}(\mathbf{x})h(t),$$

where \mathbf{f} is the external force introduced in (1). The function \mathbf{g} describes the space distribution of the source and is written in the form

$$\mathbf{g}(\mathbf{x}) = \delta(\mathbf{x} - \mathbf{x}_S)\widehat{\mathbf{w}},$$

where δ represents the Dirac distribution, \mathbf{x}_S the source location and $\widehat{\mathbf{w}}$ the direction of the applied force (cf. [16]). Alternative source distributions can be expressed in terms of gradient or curl of suitable potential functions, giving rise to pure pressure and shear waves: more complex and realistic source mechanisms are based on tensorial models (cf. [26]). The source time history is given by a Ricker-type function with maximum frequency $\nu_{max} = 3Hz$, defined as

$$h(t) = h_0[1 - 2\beta(t - t_0)^2] \exp[-\beta(t - t_0)^2], \quad (56)$$

where h_0 is a scale factor, $t_0 = 2s$ is the time shift and $\beta = \pi^2\nu_{max}^2 = 9.8696 s^{-1}$ is a parameter that determines the width of the wavelet (56). A significant property is the cut-off at both low and high frequencies: the spectrum of the signal is maximum at $\nu_p = \sqrt{\beta}/\pi$ and is practically negligible for frequencies higher than $\nu_{co} = 3\nu_p$.

In Figure 27-28, we show the two different mesh configurations. Figure 27 shows a regular, structured grid with a mesh spacing of $h \approx 40m$. The mesh size is chosen small enough to describe with sufficient precision the physical profile of the valley. Figure 28 shows an irregular, quasi-structured grid with overlap with a mesh spacing $h_1 \approx 40m$ for layer 1 (basin) and $h_2 \approx 120m$ for layer 2 (bedrock). The finest mesh is used to describe the physical boundary of the valley while the coarsest mesh the bedrock. This type of overlapping discretizations are handled by the *mortar* technique described in Section 3.1.

We assign constant material properties within each region as described in Table 7.

This regular conforming grid in Figure 27 is used with SEM discretization to produce a reference solution for the problem and provides a sufficiently accurate discretization, since further mesh refinements generates quasi-identical seismograms.

In Figures 29-30 we compare the horizontal and vertical displacement recorded

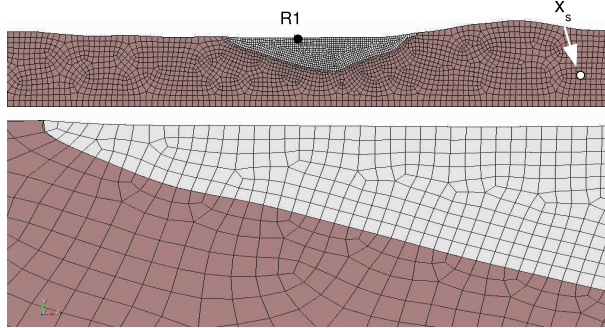


Figure 27: Conforming, structured grid with a mesh spacing of $h \approx 40$ m at the interface between the two materials. Top: receiver R1 placed on the top of the valley and point source \mathbf{x}_S within the bedrock. Bottom: zoom of the valley profile.

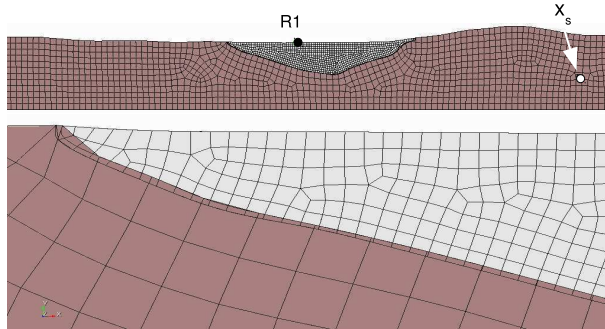


Figure 28: Non-Conforming, quasi-structured grid with overlap with a mesh spacing $h_1 \approx 40$ m for layer 1 (basin) and $h_2 \approx 120$ m for layer 2 (bedrock). Top: receiver R1 placed on the top of the valley and point source \mathbf{x}_S within the bedrock. Bottom: zoom of the valley profile.

Layer	$c_P[m/s]$	$c_S[m/s]$	$\rho[Kg/m^3]$	$\zeta[1/s]$
1	700	350	1900	0.03141
2	3500	1800	2200	0.06283

Table 5: Dynamic and mechanical parameters.

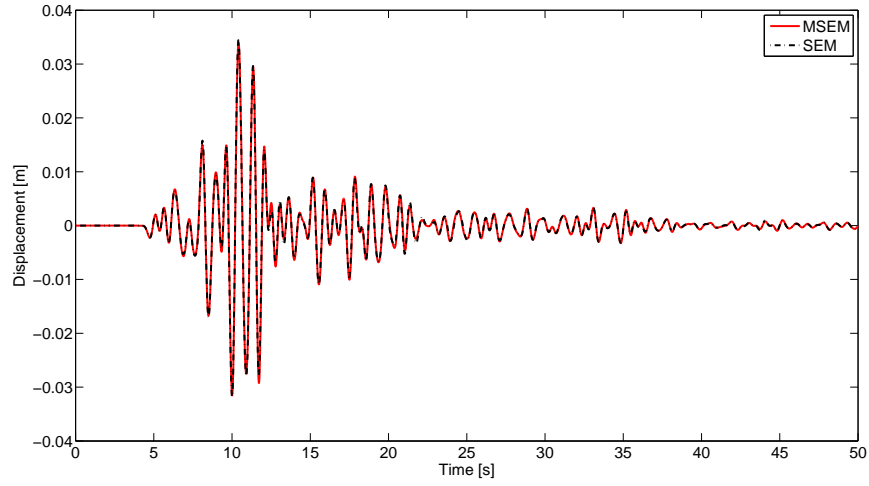


Figure 29: Horizontal displacement recorded by the receiver R1 on the free surface for the valley. Comparison between SEM and MSEM, $N=4$.

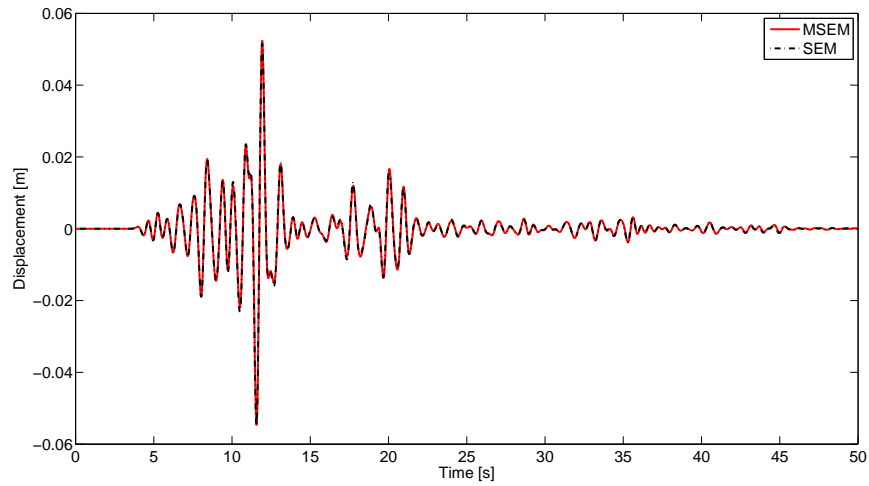


Figure 30: Vertical displacement recorded by the receiver R1 on the free surface for the valley. Comparison between SEM and MSEM, $N=4$.

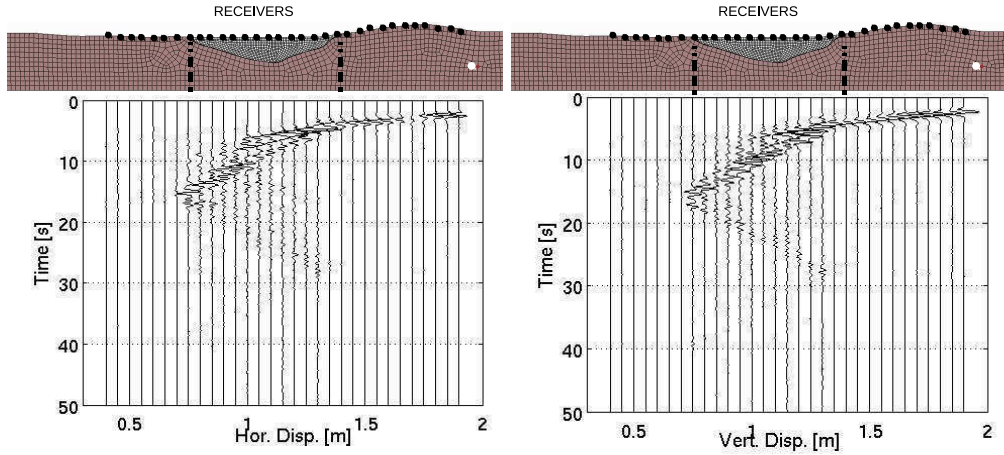


Figure 31: Time histories of the receivers on the top of the surface obtained with MSEM ($N=4$).

by receiver R1 placed on the free surface of the valley (cf. Figures 27-28). The high discontinuities between the mechanical properties of the materials produce high oscillations and perturbations on the wave front. All these complex phenomena are well captured by both SEM and MSEM using fourth order spectral elements. We remark that with MSEM we reduce the computational effort for the generation of the grid as well as the problem complexity (from 61385 spectral nodes with SEM to 48091 spectral nodes with MSEM). In Figure 31 we show the time histories of the seismograms recorded by some receivers on the free surface of the domain, obtained using MSEM. It can be observed that the wave which starts travelling from the point source remains trapped into the valley, where it is amplified and where phenomena of reflection and refraction arise. This phenomenon is relevant in some geophysical contexts, e.g. it has occurred in the Gubbio valley (in Italy) on the occasion of the earthquake of September 27, 1997. We refer to [35] for a detailed analysis.

8 Conclusions

In this paper we compared two different domain decomposition non-conforming high order numerical techniques, namely the Mortar Spectral Element Method (MSEM) and the Discontinuous Galerkin Spectral Element Method (DGSEM), for the approximation of the elastic wave equation in heterogeneous media.

Both methods preserve the spectral accuracy typical of high order methods, allow geometrically non-conforming domain partitions where local meshes are indepen-

dently generated from the neighbouring ones, and can handle variable spectral approximation degrees. Note that the subdomain partition is constructed according to the (available) material properties.

Starting from a common weak formulation we describe both approaches in order to highlight their analogies and their differences. In particular, we gave special attention to the analysis of grid dispersion, stability, and accuracy, which represent the main important features determining the applicability of a numerical method to wave propagation problems. We numerically proved that the MSEM and the DGSEM do not suffer from grid dispersion. Indeed five points per wavelength with spectral element approximations of order four are sufficient to have negligible errors. For the stability analysis we derived a precise CFL bound for the Leap-Frog scheme when employed with the considered non-conforming approaches. The threshold values obtained for the DGSEM (resp. the MSEM) are around 70 percent (resp. 95 percent) of the ones typical with the Spectral Element Method (SEM). So, on the one hand, the symmetric version of the DGSEM yields optimal error decays in the grid dispersion as occurs with the SEM. On the other hand the MSEM allows larger time step in the time advancing scheme. Finally, both non-conforming techniques are well suited for parallel computations.

References

- [1] R. A. Adams and J. F. F. Fournier. *Sobolev Spaces*, volume 140 of *Pure and Applied Mathematics*. Academic Press, New York, second edition, 2003.
- [2] M. Ainsworth. Discrete dispersion relation for *hp*-version finite element approximation at high wave number. *SIAM J. Numer. Anal.*, 42(2):553–575, 2004.
- [3] M. Ainsworth. Dispersive and dissipative behaviour of high order discontinuous Galerkin finite element methods. *J. Comput. Phys.*, 198(1):106–130, 2004.
- [4] M. Ainsworth, P. Monk, and W. Muniz. Dispersive and dissipative properties of discontinuous Galerkin finite element methods for the second-order wave equation. *J. Sci. Comput.*, 27(1-3):5–40, 2006.
- [5] P. F. Antonietti, A. Buffa, and I. Perugia. Discontinuous Galerkin approximation of the Laplace eigenproblem. *Comput. Methods Appl. Mech. Engrg.*, 195(25-28):3483–3503, 2006.
- [6] P. F. Antonietti and P. Houston. A class of domain decomposition preconditioners for *hp*-discontinuous galerkin finite element methods. *Journal of Scientific Computing*, 46:124–149, 2011.

- [7] D. N. Arnold, F. Brezzi, B. Cockburn, and L. D. Marini. Unified analysis of discontinuous Galerkin methods for elliptic problems. *SIAM J. Numer. Anal.*, 39(5):1749–1779, 2001/02.
- [8] F. Ben Belgacem and Y. Maday. A spectral element methodology tuned to parallel implementations. *Comput. Methods Appl. Mech. Engrg.*, 116(1-4):59–67, 1994.
- [9] C. Bernardi, N. Debit, and Y. Maday. Coupling finite element and spectral methods: First results. *Mathematics of Computation*, 54(189):21–39, 1990.
- [10] C. Bernardi, Y. Maday, and A. T. Patera. A new nonconforming approach to domain decomposition: the mortar element method. In *Nonlinear partial differential equations and their applications. Collège de France Seminar, Vol. XI (Paris, 1989–1991)*, volume 299 of *Pitman Res. Notes Math. Ser.*, pages 13–51. Longman Sci. Tech., Harlow, 1994.
- [11] C. Bernardi, Y. Maday, and F. Rapetti. *Discrétisations variationnelles de problèmes aux limites elliptiques*, volume 45 of *Mathématiques & Applications*. Springer-Verlag, Berlin, 2004.
- [12] C. Bernardi, Y. Maday, and F. Rapetti. Basics and some applications of the mortar element method. *GAMM-Mitt.*, 28(2):97–123, 2005.
- [13] S. C. Brenner and L. R. Scott. *The mathematical theory of finite element methods*, volume 15 of *Texts in Applied Mathematics*. Springer, Berlin, third edition, 2008.
- [14] C. Canuto, M. Y. Hussaini, A. Quarteroni, and T. A. Zang. *Spectral methods - Fundamentals in single domains*. Scientific Computation. Springer-Verlag, Berlin, 2006.
- [15] C. Canuto, M. Y. Hussaini, A. Quarteroni, and T. A. Zang. *Spectral methods - Evolution to complex geometries and applications to fluid dynamics*. Scientific Computation. Springer, Berlin, 2007.
- [16] F. Casadei, E. Gabellini, G. Fotia, F. Maggio, and A. Quarteroni. A mortar spectral/finite element method for complex 2D and 3D elastodynamic problems. *Comput. Methods Appl. Mech. Engrg.*, 191(45):5119–5148, 2002.
- [17] E. Chaljub, Y. Capdeville, and J.P. Vilotte. Solving elastodynamics in a fluid-solid heterogeneous sphere: a parallel spectral element approximation on non-conforming grids. *Journal of Computational Physics*, 187(2):457–491, 2003.
- [18] E. Chaljub, D. Komatitsch, J.P. Vilotte, Y. Capdeville, B. Valette, and G. Festa. Spectral element analysis in seismology. In Ru-Shan Wu and Valérie Maupin, editors, *Advances in wave propagation in heterogeneous*

- media*, volume 48 of *Advances in Geophysics*, pages 365–419. Elsevier - Academic Press, London, UK, 2007.
- [19] G. C. Cohen. *Higher-order numerical methods for transient wave equations*. Scientific Computation. Springer-Verlag, Berlin, 2002.
- [20] J. D. De Basabe and M. K. Sen. Stability of the high-order finite elements for acoustic or elastic wave propagation with high-order time stepping. *Geophysical Journal International*, 181(1):577–590, 2010.
- [21] J. D. De Basabe, M. K. Sen, and M. F. Wheeler. The interior penalty discontinuous galerkin method for elastic wave propagation: grid dispersion. *Geophysical Journal International*, 175(1):83–93, 2008.
- [22] J. de la Puente, M. Käser, M. Dumbser, and H. Igel. An Arbitrary High Order Discontinuous Galerkin Method for Elastic Waves on Unstructured Meshes IV: Anisotropy. *Geophysical Journal International*, 169(3):1210–1228, 2007.
- [23] M. O. Deville, P. F. Fisher, and E. H. Mund. *High-Order Methods for Incompressible Fluid Flow*. Cambridge Monographs on Applied and Computational Mathematics. Cambridge University Press, 2002.
- [24] J. Diaz and M. J. Grote. Energy conserving explicit local time stepping for second-order wave equations. *SIAM J. Sci. Comput.*, 31(3):1985–2014, 2009.
- [25] Y. Epshteyn and B. Rivière. Estimation of penalty parameters for symmetric interior penalty galerkin methods. *Journal of Computational and Applied Mathematics*, 206(2):843–872, 2007.
- [26] E. Faccioli, F. Maggio, R. Paolucci, and A. Quarteroni. 2d and 3d elastic wave propagation by a pseudo-spectral domain decomposition method. *Journal of Seismology*, 1(3):237–251, 1997.
- [27] B. Flemisch, B. Wohlmuth, F. Rapetti, and Y. Maday. Scalar and vector potentials’ coupling on nonmatching grids for the simulation of an electromagnetic brake. *COMPEL*, 24(3):1061–1070, 2005.
- [28] M.J. Grote, A. Schneebeli, and D. Schötzau. Discontinuous galerkin finite element method for the wave equation. *SIAM Journal on Numerical Analysis*, 44(6):2408–2431, 2006.
- [29] T.J.R. Hughes. *The Finite Element Method*. Prentice-Hall, 1987.
- [30] M. Käser and M. Dumbser. An Arbitrary High Order Discontinuous Galerkin Method for Elastic Waves on Unstructured Meshes I: The Two-Dimensional Isotropic Case with External Source Terms. *Geophysical Journal International*, 166(2):855–877, 2006.

- [31] D. Komatitsch and J. Tromp. Introduction to the spectral-element method for 3-D seismic wave propagation. *Geophys. J. Int.*, 139(3):806–822, 1999.
- [32] Y. Maday, C. Mavriplis, and A. T. Patera. Nonconforming mortar element methods: application to spectral discretizations. In *Domain decomposition methods (Los Angeles, CA, 1988)*, pages 392–418. SIAM, Philadelphia, PA, 1989.
- [33] Y. Maday, F. Rapetti, and B. I. Wohlmuth. Mortar element coupling between global scalar and local vector potentials to solve eddy current problems. In *Numerical mathematics and advanced applications*, pages 847–865. Springer Italia, Milan, 2003.
- [34] K.J. Marfurt. Accuracy of finite-difference and finite-element modeling of the scalar and elastic wave equations. *Geophysics*, 49(5):533–549, 1984.
- [35] I. Mazzieri, R. Paolucci, C. Smerzini, and M. Stupazzini. In preparation. 2011.
- [36] R. Mullen and T. Belytschko. Dispersion analysis of finite element semidiscretizations of the two-dimensional wave equation. *Internat. J. Numer. Methods Engrg.*, 18(1):11–29, 1982.
- [37] A. Quarteroni, R. Sacco, and F. Saleri. *Numerical mathematics*, volume 37 of *Texts in Applied Mathematics*. Springer-Verlag, Berlin, second edition, 2007.
- [38] A. Quarteroni and A. Valli. *Numerical approximation of partial differential equations*, volume 23 of *Springer Series in Computational Mathematics*. Springer-Verlag, Berlin, 1994.
- [39] F. Rapetti. An overlapping mortar element approach to coupled magneto-mechanical problems. *Mathematics and Computers in Simulation*, 80(8):1647–1656, 2010.
- [40] P.-A. Raviart and J.-M. Thomas. *Introduction à l'analyse numérique des équations aux dérivées partielles*. Collection Mathématiques Appliquées pour la Maîtrise. Masson, Paris, 1983.
- [41] B. Rivière. *Discontinuous Galerkin methods for solving elliptic and parabolic equations - Theory and implementation*, volume 35 of *Frontiers in Applied Mathematics*. Society for Industrial and Applied Mathematics (SIAM), Philadelphia, PA, 2008.
- [42] B. Rivière, S. Shaw, M. F. Wheeler, and J. R. Whiteman. Discontinuous Galerkin finite element methods for linear elasticity and quasistatic linear viscoelasticity. *Numer. Math.*, 95(2):347–376, 2003.

- [43] B. Rivière and M. F. Wheeler. Discontinuous finite element methods for acoustic and elastic wave problems. In *Current trends in scientific computing (Xi'an, 2002)*, volume 329 of *Contemp. Math.*, pages 271–282. Amer. Math. Soc., Providence, RI, 2003.
- [44] D. Sármany, M. A. Botchev, and J. J. W. van der Vegt. Dispersion and dissipation error in high-order Runge-Kutta discontinuous Galerkin discretisations of the Maxwell equations. *J. Sci. Comput.*, 33(1):47–74, 2007.
- [45] G. Seriani and S. P. Oliveira. Dispersion analysis of spectral element methods for elastic wave propagation. *Wave Motion*, 45(6):729–744, 2008.
- [46] G. Seriani, E. Priolo, and A. Pregarz. Modelling waves in anisotropic media by a spectral element method. In G. Cohen, editor, *Proceedings of the third international conference on mathematical and numerical aspects of wave propagation*, pages 289–298. SIAM, Philadelphia, PA, 1995.
- [47] R. Stacey. Improved transparent boundary formulations for the elastic-wave equation. *Bulletin of the Seismological Society of America*, 78(6):2089–2097, 1988.
- [48] D. Stanescu, D. A. Kopriva, and M. Y. Hussaini. Dispersion analysis for discontinuous spectral element methods. *J. Sci. Comput.*, 15(2):149–171, 2000.

MOX Technical Reports, last issues

Dipartimento di Matematica “F. Brioschi”,
Politecnico di Milano, Via Bonardi 9 - 20133 Milano (Italy)

- 14/2011 ANTONIETTI, P.F.; MAZZIERI, I.; QUARTERONI, A.; RAPETTI, F.
Non-Conforming High Order Approximations for the Elastic Wave Equation
- 13/2011 LOMBARDI, M.; PAROLINI, N.; QUARTERONI, A.; ROZZA, G.
Numerical simulation of sailing boats: dynamics, FSI, and shape optimization
- 12/2011 MIGLIO E.; CUFFARO M.
Tectonic evolution at mid-ocean ridges: geodynamics and numerical modeling
- 11/2011 FORMAGGIA, L.; MINISINI, S.; ZUNINO, P.
Stent a rilascio di farmaco: una storia di successo per la matematica applicata
- 10/2011 ZUNINO, P.; VESENTINI, S.; PORPORA, A.; SOARES, J.S.; GAUTIERI, A.; REDAELLI, A.
Multiscale computational analysis of degradable polymers
- 09/2011 FIGOLI, D.; SANGALLI, L.
Wavelets in Functional Data Analysis: estimation of multidimensional curves and their derivatives
- 08/2011 IEVA, F.; PAGANONI, A.M.; SECCHI, P.
Mining Administrative Health Databases for epidemiological purposes: a case study on Acute Myocardial Infarctions diagnoses
- 07/2011 ARIOLI, G.; GAMBA, M.
Automatic computation of Chebyshev polynomials for the study of parameter dependence for hyperbolic systems
- 06/2011 SECCHI, P.; STAMM, A.; VANTINI, S.
Large p Small n Data: Inference for the Mean
- 05/2011 ARIOLI, G.; GAMBA, M.
An algorithm for the study of parameter dependence for hyperbolic systems